Politecnico
di Torino

1859

Synthesis and Characterization of Copper-Silver Bimetallic Cathodes for Electroreduction of Carbon Dioxide

Master of Science course in Materials Engineering

Author: Felicia Di Costola

Supervisor: Giancarlo Cicero
Co-supervisor: Juqin Zeng

A.Y. 2022-2023

Contents

Introduction

The need to reduce the emissions of CO_2, a dangerous greenhouse gas and a common waste of industrial processes, is increasingly pressing with the goal of achieving carbon neutrality by 2050, as established by the Paris Agreement. Many strategies have been developed in recent years in the context of Carbon Capture Utilization and Storage (CCUS) to achieve this goal, and prominent among them is the CO_2 Reduction Reaction (CO_2RR). This process involves the electrochemical transformation of CO_2 into high-value products that can be used as fuels or chemical reagents such as hydrocarbons and alcohols, with the advantage of reducing CO_2 emissions to the environment. This is possible by supplying electricity to the experimental setup (electrochemical cell), in which the reduction reactions take place at the cathode. Although, the process would seem rather simple, in the reality it presents many problems. Firstly, CO_2 is a very thermodynamically stable gas and therefore difficult to reduce; this makes the reduction process an energy intensive one. For this and other reasons, it is fundamental to deposit a catalyst material on the cathode to increase the efficiency of the process. Among the materials used for this application, copper stands out for its unique ability to reduce CO_2 into high energy-density products (hydrocarbons and alcohols). The biggest issue with this material is its low selectivity for a single product, which complicates the separation between the different generated chemical compounds. Many structural and functional modifications have been made to copper-based catalysts in order to improve their electrocatalytic behavior. One possibility is to couple another metal to Cu creating bimetals or alloys. The idea behind these designs is to achieve a synergistic effect between the two metals to obtain better selectivity and activity.

This thesis project has the aim to research and study innovative catalysts to obtain high-value products by reducing CO_2. In particular, the work aims at exploiting the ability of copper bimetallic compounds that, when employed as electrodes in electrochemical cells, have the capability to catalyze the chemical reactions of interest. The activity of this work can be divided in three main sections: (i) synthesis of bimetallic compounds, (ii) electrochemical characterization of the obtained samples, (iii) structural and chemo-physical characterization of the bimetallic synthetized material.

The purpose of the first part of work was the realization of the electrode materials.

The attention has been focused on the study of bimetallic copper-silver to obtain a cooperative effect between these two metals. The production of these alloys started with sputtering deposition of copper on carbon paper (gas diffusion layer). Afterwards, the surface copper was (partially) replaced by silver through a displacement reaction in silver sulfate (Ag_2SO_4) aqueous solution. The intent was to optimize the material performance reaching the best activity and selectivity to C_2 products (ethanol, acetic acid, ethylene). To obtain suitable material properties, different temperatures and durations of immersion of the Cu-based specimen in the reaction bath were used.

Following, we studied the bimetallic catalyst behaviour during CO_2 reduction via electrochemical measurements. In this specific case, the experimental setup consisted of a three-electrode cell in which the working electrode was obviously the cathode. Several galvanostatic tests were performed for each sample using different current densities with the intent of understanding how the material performance would vary when converting carbon dioxide into organic feedstocks. High-performance liquid chromatography (HPLC) and gas chromatography (GC) have been used to estimate the amount of liquid and gaseous products, respectively and these values were then employed to calculate the Faradaic efficiencies (FE).

Characterizations of fresh samples were performed by making use of Field Emission Scanning Electron Microscopy (FESEM). Precisely, there are two main reasons for which this type of analysis was important in this study. First, we investigated the morphology and surface structure of the obtained material and by means of Energy Dispersive Spectroscopy (EDX or EDS) technique, we obtained the Ag/Cu ratios at the catalysts surfaces prepared in different conditions. Finally, X-ray diffraction (XRD) analysis was used to understand how the material is organized from the crystallographic point of view.

The activities described above have yielded interesting results and the examined material has showed high C_2 production. The operating principle on which Ag-Cu coupling is based is called *tandem effect* or *CO spillover*. The goal is to promote the carbon monoxide (CO) adsorption on Cu surface thanks to the presence of silver, a metal that presents notable selectivity for converting CO_2 to CO and, in this way, enhances electrode selectivity for multicarbon (C_2) products through CO dimerization. Further experimental work is needed for a mechanistic understanding of the molecular processes occurring at the catalyst surface by using for example in situ Raman spectroscopy and in situ X-ray photoelectron spectroscopy (XPS). Future optimization of the catalysts studied in this thesis work may consist of the employment of Cu nanoparticles rather than sputtered Cu. This would possibly lead to an increase of the catalyst active surface area and thus to a higher reduction yields.

The thesis is organized as follows. In Chapter 1 a description of the electrochemical

CO_2 reduction process is given and the state of the art of the most commonly used catalysts in this field is summarized, with a focus on copper and copper-silver based bimetallic compounds. Chapter 2 presents the methods used during the experimental work for the synthesis and the electrochemical/material characterization of the Cu-Ag bimetallic cathodes studied. The experimental results obtained in the framework of this thesis are shown and discussed in Chapter 3, and finally in Chapter 4, conclusions and future perspectives are presented.

CHAPTER 1

Carbon Dioxide Electroreduction: an overview

In this first introductory chapter, a preliminary description of the electrocatalytic CO_2 reduction process will be provided, highlighting its potential and critical issues. This will then be followed by a summary of the classes of materials used as catalysts for the reduction reactions of interest, specifically focusing on single and bimetallic copper-based catalysts.

1.1 Close the carbon cycle: dream or reality?

CO_2 is a dangerous greenhouse gas (GHG) which, together with water vapor (H_2O), methane (CH_4), nitrous oxide (N_2O) and ozone (O_3), contributes to global warming and in general, to climate change. With a view to a careful environmental policy, it becomes important to reduce the carbon footprint and the global temperature with the final aim of reaching carbon neutrality by 2050 according to Paris Agreement [1, 2]. In Figure1.1 is represented the desirable evolution of CO_2 emissions with respect to the time, obtainable thanks to various solutions.

In the last years, new technologies and processes are being developed to produce renewable energy with high efficiency and consequently, reduce the amount of emissions in the atmosphere. But hydrocarbons are still essentials to storage energy and, in order to reach ”defossilization”, the search for new ways to produce these feedstocks from renewable electricity and water is carried out. In this area of research hydrogen production from water splitting stands out for instance but both storage and transport of this gas is really critical and very difficult. Moreover, the high cost of hydrogen conversion of the existing energy infrastructures must be take into account. For these and others reasons, carbon capture utilization and storage (CCUS) has attracted a lot of attention being the main way to recycle CO_2 captured from the atmosphere and use it as carbon source for the generation of molecules like methane, ethanol and more. There

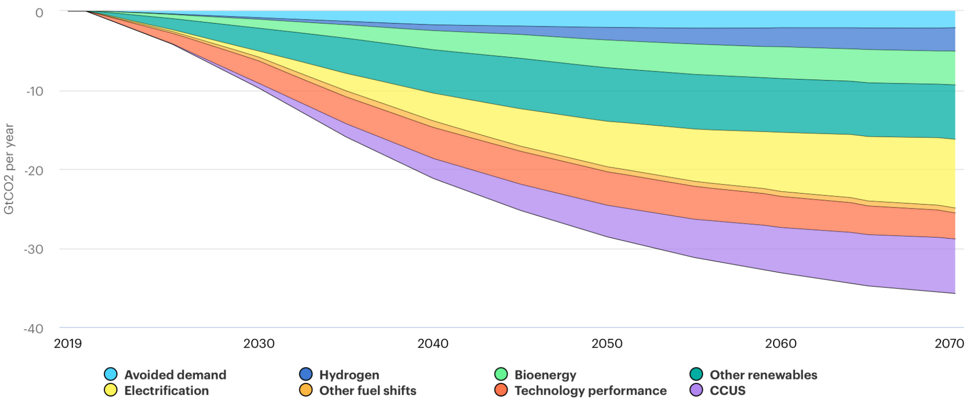

IEA. All rights reserved.

Figure 1.1: Global energy sector CO_2 emissions reductions by measure in the Sustainable Development Scenario relative to the Stated Policies Scenario, IEA, Paris [3].

are many different pathways to synthetize CO_2-based molecules, as shown in Figure1.2. Specifically, mineralization consists in converting alkaline compounds mixed with CO_2 into solid carbonates. Using microorganisms, CO_2 can be reduced in biomass and feedstocks through biological process. When working with catalysts, thermocatalytic hydrogenation at high temperature and pressure or electrochemical reduction of CO_2 (CO_2RR) providing electricity into an electrochemical cell, are both valid alternatives. Moreover, some semiconductors make it possible to use light irradiation from the Sun for the photo-electrochemical reduction (PEC) of CO_2.

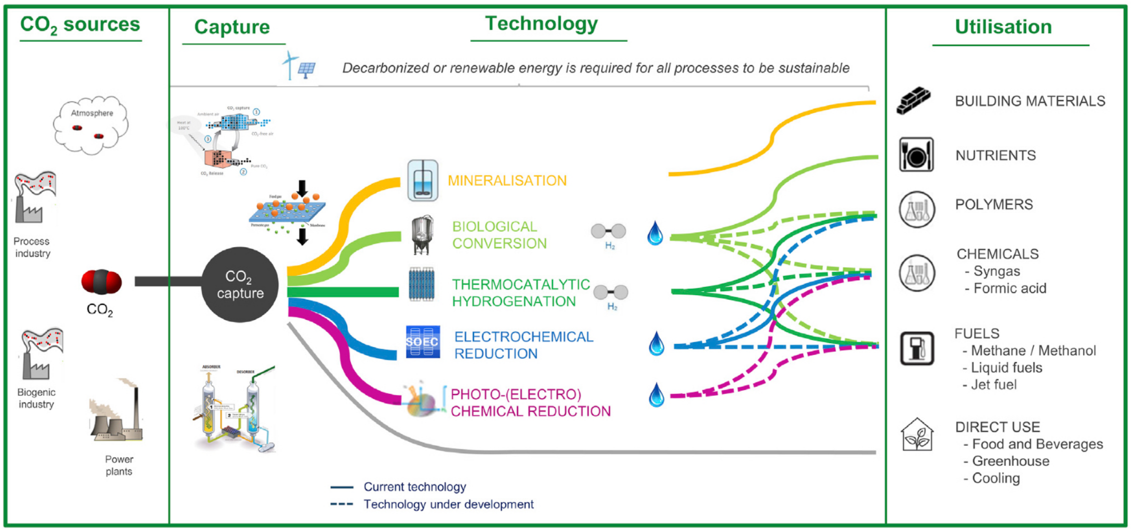

Figure 1.2: Different chemical and biological pathways to produce CO_2-based e-molecules [1].

1.2 CO_2 electrochemical reduction

Electrocatalytic reduction (ECR) of CO_2, as discussed before, is an emerging process that needs to be studied and optimized in lab scale in order to become an alternative way to long-term storage of energy. Firstly, CO_2 is a very thermodynamically stable and fully oxidized compound and it exhibits a strong double bond C=O (750 kJ/mol) [4]. The features of this molecule make its reduction, characterized by high activation barrier and overpotential, very hard. Another inconvenience is given by the presence of many different possible reaction intermediates due to the multi-electron and proton transfers in aqueous electrolyte (Figure1.3) leading to the difficult understanding and prediction of all the phenomena happening during the electrolyzer operation.

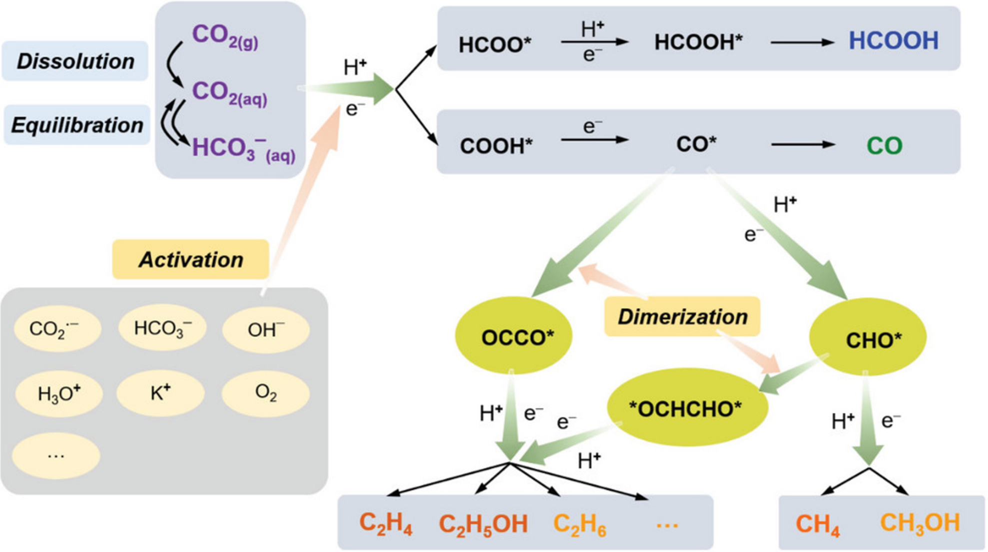

Figure 1.3: Proposed surface reaction pathways and mechanism of CO_2RR to valuable products [5].

Before looking deeply into this process, it is necessary to introduce some important parameters used to measure the performance of electrocatalysis [6, 7]. In order to quantify the selectivity, defined as the capacity to obtain one specific product from the reactants, the Faradaic efficiency (FE) is applied. It is defined as the amount of collected product relative to the amount that could be produced from the total charge passed. Applied potential represents the practical electrode potential; the difference between the equilibrium and the applied potential is called overpotential. To exstimate the quantity of energy employed for a product the energetic efficiency (EE) is used, which relates the stored energy of the product to the energy consumed to generate it. The catalytic activity can be valued using TOF (turn-over frequency), defined as the quantity of the product generated per active site per unit time. Furthermore, specific current density reflects the reduction kinetics and can be calculated as the ratio between the geometric current intensity and the electrochemical active surface area (ECSA).

With that being said, ECR consists of five main phases[8]: (i) CO_2 and protons diffusion from bulk electrolyte to electrode surface; (ii) CO_2 adsorption and activation on catalyst surface; (iii) multi-electron/proton transfer in order to generate intermediates; (iv) interactions between intermediates and desorption as final products; (v) diffusion into the bulk electrolyte. As previously anticipated, CO_2 activation is very difficult because of the need to overcome a large energy barrier and form $^*CO_2{}^-$ intermediate thanks to the application of a negative potential of -1.90 V vs the standard hydrogen electrode (SHE) [6, 8]. In Figure1.4 [4] all the obtainable products, the corresponding equations with the number of electrons required for the reaction and the standard potentials are summarized.

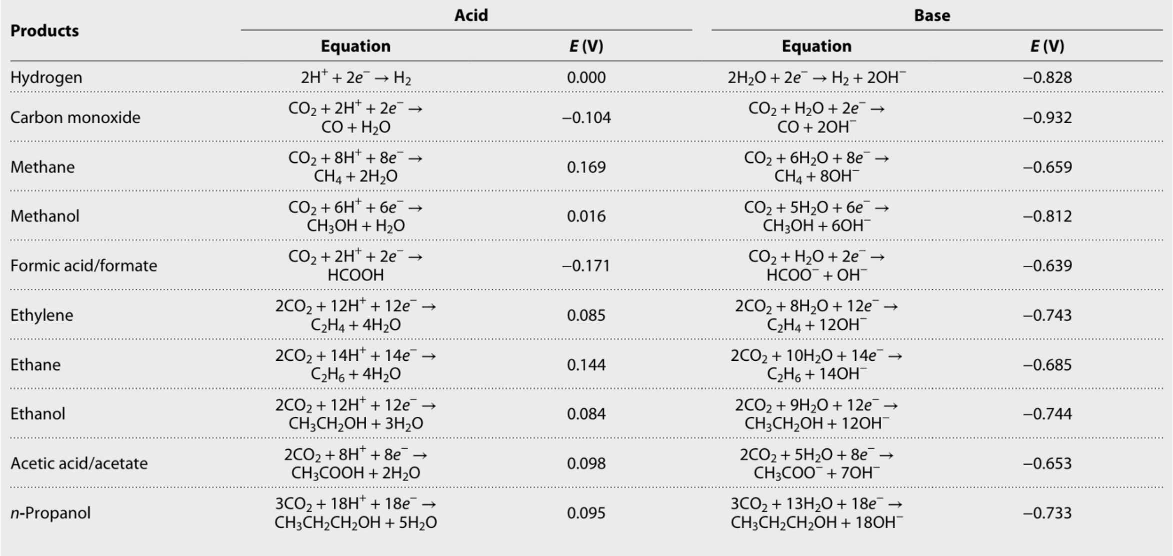

Products	**Acid**		**Base**	
	Equation	***E* (V)**	**Equation**	***E* (V)**
Hydrogen	$2H^+ + 2e^- \rightarrow H_2$	0.000	$2H_2O + 2e^- \rightarrow H_2 + 2OH^-$	−0.828
Carbon monoxide	$CO_2 + 2H^+ + 2e^- \rightarrow CO + H_2O$	−0.104	$CO_2 + H_2O + 2e^- \rightarrow CO + 2OH^-$	−0.932
Methane	$CO_2 + 8H^+ + 8e^- \rightarrow CH_4 + 2H_2O$	0.169	$CO_2 + 6H_2O + 8e^- \rightarrow CH_4 + 8OH^-$	−0.659
Methanol	$CO_2 + 6H^+ + 6e^- \rightarrow CH_3OH + H_2O$	0.016	$CO_2 + 5H_2O + 6e^- \rightarrow CH_3OH + 6OH^-$	−0.812
Formic acid/formate	$CO_2 + 2H^+ + 2e^- \rightarrow HCOOH$	−0.171	$CO_2 + H_2O + 2e^- \rightarrow HCOO^- + OH^-$	−0.639
Ethylene	$2CO_2 + 12H^+ + 12e^- \rightarrow C_2H_4 + 4H_2O$	0.085	$2CO_2 + 8H_2O + 12e^- \rightarrow C_2H_4 + 12OH^-$	−0.743
Ethane	$2CO_2 + 14H^+ + 14e^- \rightarrow C_2H_6 + 4H_2O$	0.144	$2CO_2 + 10H_2O + 14e^- \rightarrow C_2H_6 + 14OH^-$	−0.685
Ethanol	$2CO_2 + 12H^+ + 12e^- \rightarrow CH_3CH_2OH + 3H_2O$	0.084	$2CO_2 + 9H_2O + 12e^- \rightarrow CH_3CH_2OH + 12OH^-$	−0.744
Acetic acid/acetate	$2CO_2 + 8H^+ + 8e^- \rightarrow CH_3COOH + 2H_2O$	0.098	$2CO_2 + 5H_2O + 8e^- \rightarrow CH_3COO^- + 7OH^-$	−0.653
n-Propanol	$3CO_2 + 18H^+ + 18e^- \rightarrow CH_3CH_2CH_2OH + 5H_2O$	0.095	$3CO_2 + 13H_2O + 18e^- \rightarrow CH_3CH_2CH_2OH + 18OH^-$	−0.733

Figure 1.4: Possible obtainable products from ECR both in acidic and basic reaction environment (Potentials refer to the SHE, pH = 0 for acid and pH = 14 for base) [4].

It is possible to see the general trend in which as the number of carbon atoms in the specific compound increases, the number of the electrons required increases and the standard potential vs reversible hydrogen electrode (RHE) becomes more positive. However, while the interpretation of the C_1 products formation is at a good point and validated by theoretical calculations, the same cannot be said for C_{2+} because of the existence of different possible pathways with the most important ones schematized in Figure1.5. This also explains the difficulty in obtaining high selectivity that in the state-of-art is around $60-70\%$ FE towards C_2 [9, 10] and 30% FE towards C_3 [11].

Therefore, considering the greater energy density of multi-carbon feedstocks and the many issues encountered during their production, many efforts to improve the electrolyzer performances have been made. Some of these catalyst design strategies can be: creation of alloys, morphological modification of cathode surface involving doping atoms or defects, the tuning of the crystalline orientation and of the oxidation state [4]. The scientific area concerned in the study of performance-enhancing methods is called

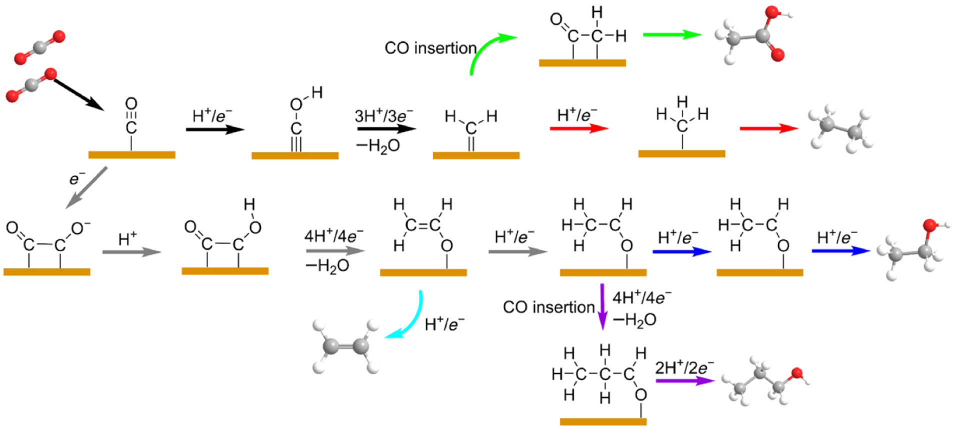

Figure 1.5: Most important possible C_{2+} pathways during ECR [4, 12].

electrocatalytic surface and near-surface engineering (ESE) and it covers six aspects (Figure1.6): bulk compositions and structures of catalytic materials, catalyst supports, surface catalytic sites, catalyst reconstructions, surface modification and protections and local electrolyte environment [5].

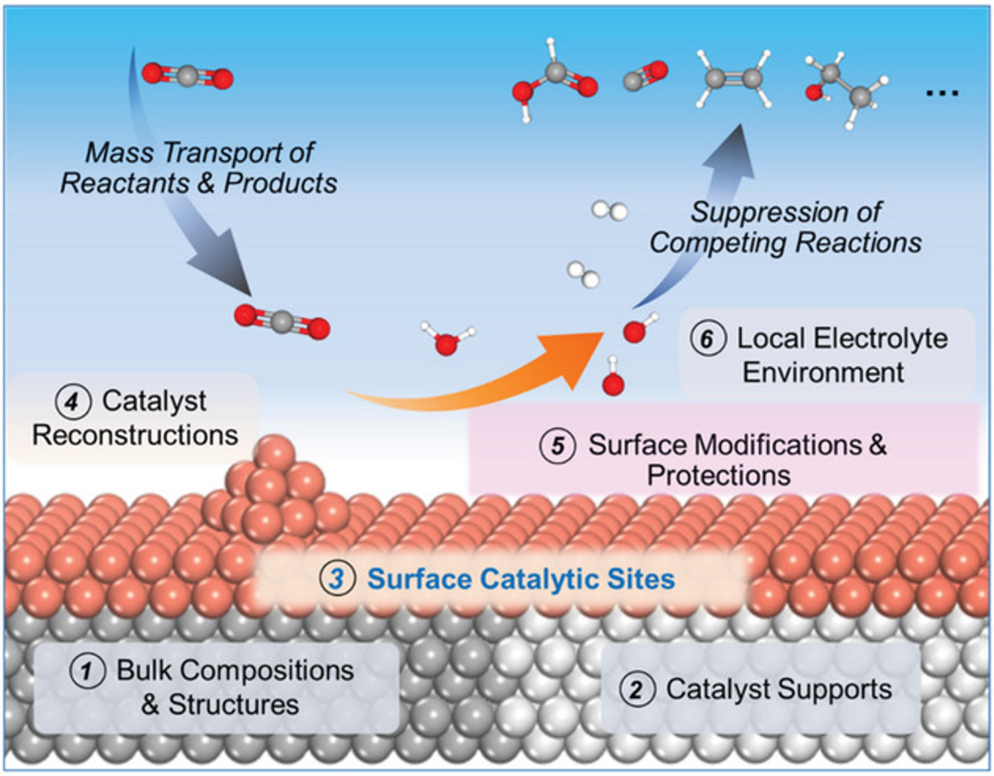

Figure 1.6: ESE six main areas of operation [5]

1.2.1 Design of electrochemical cell

It has already been clarified that ECR process takes place into a particular device, called electrolyzer, in which electrical energy is converted into chemical transformations (Figure 1.7), and its optimization could be essential in order to increase catalytic performances. In general, the anode is where oxygen evolution reaction (OER) takes place, employing water as reactant and producing molecular oxygen, protons and electrons 1.1. The latter are useful for reduction reactions developing at the cathode.

$$2H_2O \rightarrow 4\text{e}^{-} + 4H^{+} + O_2 \tag{1.1}$$

Therefore, the presence of an ion exchange membrane becomes indispensable in order to avoid the oxidation of the products formed at the cathode, allowing the passage of protons only. [13].

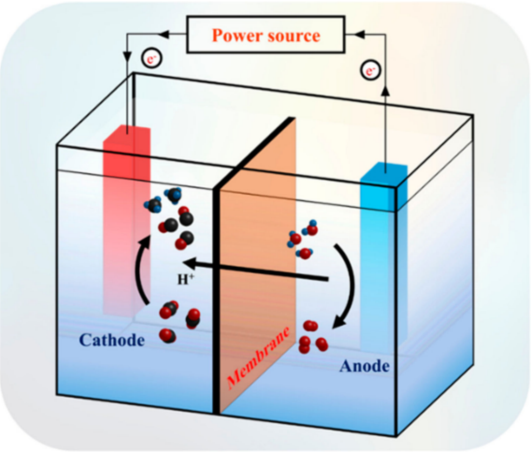

Figure 1.7: Schematic illustration of electrochemical cell used for CO_2RR[13].

Different kinds of electrolyzer configurations have been developed: H-type cell, polymer electrolyte membrane flow cell, solid oxide electrolysis cell (SOEC) and differential electrochemical mass spectrometry (DEMS) cell [14]. In an H-type cell, the cathode (working electrode) together with the reference electrode are in a chamber separated from the anode (counter electrode) by an ion-exchange membrane. The CO_2 flows into cathodic compartment which produces a major drawback represented by the low CO_2 solubility of $0.034M$ [4]. Other inconveniences are the limited electrode surface area and the large electrode distance. Despite these disadvantages, it remains the most widely used cell in lab because of its cheapness and ease. To compensate these criticalities, the polymer electrolyte membrane (PEM) flow cell was proposed. It is considered more convenient for large-scale (industrial) applications for its ability to reduce mass transfer limitations to reach higher current densities (above $100mA/cm^2$). The configuration is similar to the proton exchange membrane fuel cells (PEMFC) and the main difference is that the cathode and the anode are separated but sufficiently close to decrease the cell resistance. In addition, the catalysts are deposited on a gas diffusion layer (GDL) that, thanks to its microporosity, leads to higher surface areas resulting in higher current densities. The membrane used in this setup can be a cation-exchange membrane (CEM), an anion-exchange membrane (AEM) or a bipolar membrane (BPM). Alternatively, in 2010 the microfluidic flow cell was proposed by Kenis [15] in which, instead of the membrane, the two electrodes are separated by a thin electrolyte layer. Finally, SOEC is used at high temperature to improve the kinetic and in this way obtain high efficiency without precious metal catalysts while DEMS is based on pervaporation membrane with the aim to collect and analyze products in real time.

1.2.2 Advantages and challenges of CO_2RR

In the last decades, CO_2RR has been studied because of its various advantages: the low environmental impact of the process that generates high-value added feedstocks, by using renewable energies as solar and wind, the possibility to recycle the electrolyte generating only wastewater, the ease of scaling-up the devices and controlling the process through potentials and reaction temperature. However, the several challenges cannot be neglected. In fact, it is very hard to reach high selectivity, activity and long-term stability for this kind of process and for these reasons many efforts have been made in order to achieve these goals. Some of the main critical issues are: the slow kinetics of reduction, the low energy efficiency due, for instance, to parasitic reactions like the hydrogen evolution (HER), which shows a close potential (-0.42 V vs SHE, pH $= 7$) [6] compared with ECR of CO_2 reactions, or to the risk of electrode poisoning [16, 17].

1.3 State-of-art in CO_2RR materials

In this section, the aim is to summarize the state-of-art of catalyst materials used as cathode during CO_2RR. It is possible to distinguish three typologies of catalysts: metallic, non-metallic and molecular [17]. During this paper the focus will be on metal catalysts and specifically copper-based catalysts so as to clarify some useful aspects for understanding the following study. Metal based catalysts can be divided into four different classes of materials [8, 17]:

1. based on Au (gold), Ag (silver), Pd (palladium), Ga (gallium) and Zn (zinc) which are selective towards CO because they favor the generation of $^{*}COOH$;
2. based on Pb (lead), In (indium), Sn (tin), Hg (mercury), Cd (cadmium), Tl (thallium) and Bi (bismuth), selective to formate thanks to the ability of promoting the formation of *HCOO;

3. based on Pt (platinum), Fe (iron), Ni (nickel) and Ti (titanium) that are able to produce mainly hydrogen;
4. based on Cu (copper), characterized by scaling relationship with reaction intermediates [18] that gives low selectivity but, on the other hand, they are the only catalysts able to produce hydrocarbons like methane and ethylene with good Faradaic efficiencies [19, 20].

1.3.1 Cu-based catalysts: a review

To fully understand the copper uniqueness, it is appropriate to give an idea of which mechanisms happen on the electrode surface during the CO_2 reduction (Figure1.8). The description of these phenomena is very complex since this material is capable of producing 16 compounds from CO_2 among which are also included multi-carbon aldehydes, ketones and alcohols. Firstly, regarding C_1 chemicals, formate ($HCOO^*$) or carboxyl ($COOH^*$) intermediates are generated via proton/electron pair trasfer and these species can be reduced to HCOOH (formic acid) thanks to a second proton transfer. But carboxyl can also lead to CO (carbon monoxide) while formate can give H_2COO^* (biformate). CO intermediates can produce CH_4 or CH_3OH through "carbene" species ($^*CH_2$). "Carbene" mechanism is also proposed for C_2 and proceeds thanks to dimerization or CO insertion. Another way to explain the C_2 pathway on copper is the hydrogenation of $^*CO$ in order to give $^*HCO$, $^*H_2CO$ and $^*H_3CO$, followed by the dimerization of these species and the consequent deoxygenation to produce ethylene. [19, 21, 22].

Since copper and copper-base electrodes are the only ones able to produce high quantity of C_2 chemicals but with low selectivity, the research on this material focuses on its optimization with the aim of achieving high productivity towards high energy-density products as ethanol or ethylene. Many strategies have been studied: the effect of compressive/tensile strain, the introduction of a second element, the control of the surface morphology, etc [8, 23, 24]. Some of the effects found in literature will now be summarized. With regard to the coordination environment, it was found that if Cu nanoparticles have a size smaller than 5 nm, the production of H_2 and CO increases while the quantity of hydrocarbons decreases. In contrast, selectivity towards hydrocarbons rises if inter-particle distance is shorter than that [25]. Additionally, crystalline orientation of Cu surface atoms can influence the selectivity and in particular (100)[1] facet of Cu leads to ethylene while (111) facet gives methane.

Other important ways to increase C_{2+} are the creation of an higher surface area obtainable through an higher level of porosity and the introduction of defects obtainable through doping, etching or partial oxidation of the surface that can suppress the HER and increase selectivity toward specific chemicals [8, 26]. Also, the promotion of C-C

---

[1] Crystalline plane family

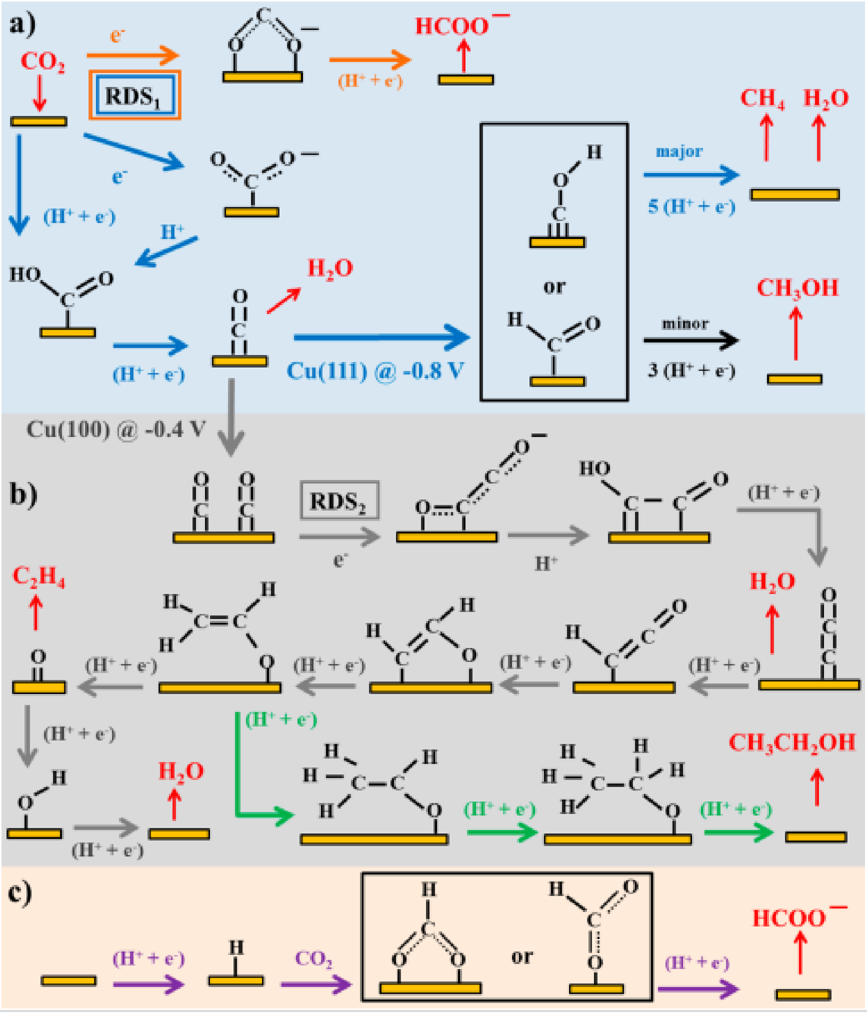

Figure 1.8: Reaction pathways on copper to (a) CO, CH_4, CH_3OH; (b) ethylene and ethanol; (c) formate [19].

coupling and the consequent C_2H_4 selectivity can be attained taking advantage of the synergy between Cu^0 and Cu^+ obtained by the presence of copper in oxidized matrix [27] while alcohol selectivity can be improved controlling *CO surface coverage [28]. The reduction products can be controlled by varying the adsorption energy of *CO through the regulation of the electronic structure adding to the pure Cu a second component, obtaining an alloy or a surface strain. Regarding the strain effect, two theories have been modeled: the d-band model (by Norskov) and the eigenstress model (by Peterson). The first of them assumes that when a surface expansion occurs, the result is a narrow d-band which gives a stronger adsorption while the second one provides that the scaling relationships can be broken by the strain [8]. Another very relevant aspect which makes the behavior of copper unpredictable is its reconstruction during ECR under a negative bias [29] and for this reason it is essential to characterize the surface while the material is working using in operando/in situ techniques. Also some extrinsic factors, as the local environment, can have an effect on reaction pathways in CO_2 ECR. For instance, local CO_2 concentration used in flow electrolyzer based on GDEs can be modulated in order to increase the C-C coupling on Cu_2O NPs [30]. In particular, catalysts layer thickness and porosity, feed flow rate and CO_2 feed concentration can change the local CO_2 concentration and, as shown in Figure1.9, multi-carbon product selectivity is at its maximum using moderate local CO_2 concentration.

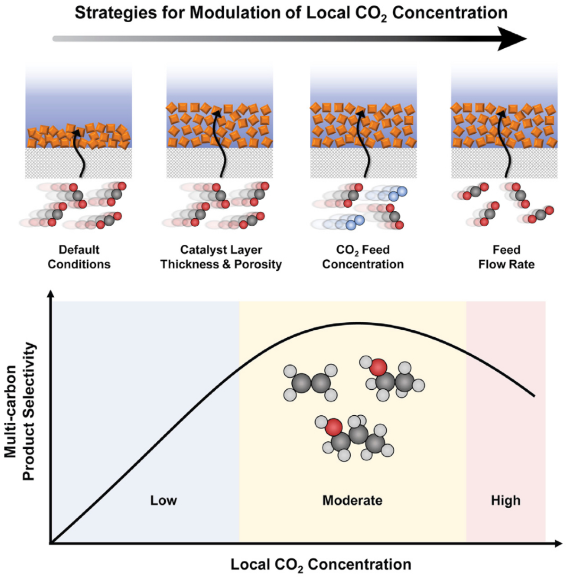

Figure 1.9: Ways to tune local CO_2 concentration and its influence on C-C coupling [30].

1.4 Bimetallic catalysts in CO_2RR

Previously it has already been emphasized the importance of the electrocatalytic processes like oxygen reduction reaction (ORR) and carbon dioxide reduction (CO_2RR). The state-of-art of catalysts is based on Pt for ORR and on Cu for CO_2RR (Figure 1.10) and the research on this field proposes the developing of bimetallic alloys adding a second metal to Pt and Cu in order to achieve the best performances in both the electrochemical processes [31].

As far as this thesis work is concerned, in the next subsection the focus will be on Cu-based bimetallic catalysts and in particular on Ag-Cu bimetallics, which are the main protagonists of this experimental study.

1.4.1 Cu-based bimetallic catalysts for CO_2RR

The main goals that are hoped to achieve employing bimetallic materials are the reduction of the overpotential and the increase of the activity and the total FE. The major

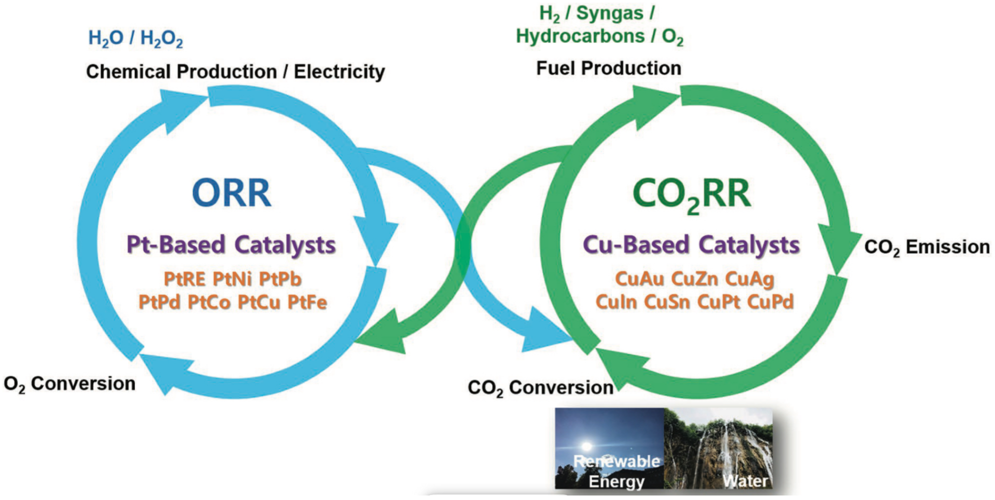

Figure 1.10: Comparison between ORR and CO_2RR[31].

advantageous features 1.11 to which they lead are: (i) the less need of noble metals (Ag, Au, etc.) due to the coupling with Cu, (ii) the modification of the pure metal electronic structure that can optimize the binding strength between the intermediates and the electrode, following the Sabatier principle for which the bond must be neither too weak nor too strong in order to favour the C-C coupling between intermediates but not incurring in CO poisoning, (iii) the creation of new active sites and (iv) the tandem catalysis which makes possible the conduct of multiple reactions in one single device, reducing wastes and costs [7].

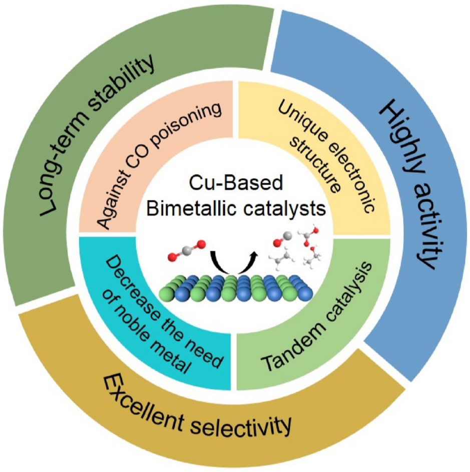

Figure 1.11: Advantages of copper-based bimetallic catalysts[7]

The most used Cu alloy nanocatalysts will now be briefly described. It is possible to distinguish them in three classes according to the main product generated by the added metal: with formate-producing metals (Sn, In, Bi), with CO-producing metals (Au, Ag, Zn) and H_2 producing-metals (Pt, Pd) [31].

Sn-Cu bimetallic catalysts allow to obtain, at lower overpotentials and with better stability, the same selectivity towards formate shown by Sn-based materials cited above 80% FE [32, 33]. It is possible to use, for instance, a core-shell structure or to increase Sn content disfavoring CO in favor of formate generation [7].
In-Cu bimetallic catalysts give the possibility to generate selectively CO (95% FE) depositing In on oxide-derived Cu (OD-Cu) [34] or alternatively it can produce syngas with different CO/H_2 ratios modulating In content on Cu nanostructures [35].
Bi-Cu bimetallic catalysts allow to decrease the overpotential, ensuring the high selectivity to formate/formic acid characteristic of Bi-based materials ($>$ 90% FE) [36, 37].
Au-Cu bimetallic catalysts exhibits high selectivity towards C_{2+} products taking advantage of the tandem catalysis [38] or, coupling Au and Cu NPs with an organic ligand [39].
Ag-Cu bimetallic catalysts, similar to Au-Cu alloys, can lead to the generation of C_{2+} products through tandem effect or CO spillover for which Ag converts CO_2 to CO near to Cu surface creating high CO coverage that induces C-C coupling [40], as shown in Figure1.12[41]. As opposed to the previous theory, this selectivity may be due to the compressive strain effect caused by Ag doping on Cu surface. As consequence, Cu remains the active site and it is observed that the Cu valence band shift leads to the decrease of adsorption energies of hydrogen and oxygen resulting in the inhibition of the HER and in the favoured absorption of CO [42]. Some other considerations about this type of catalyst will be made in the next section.

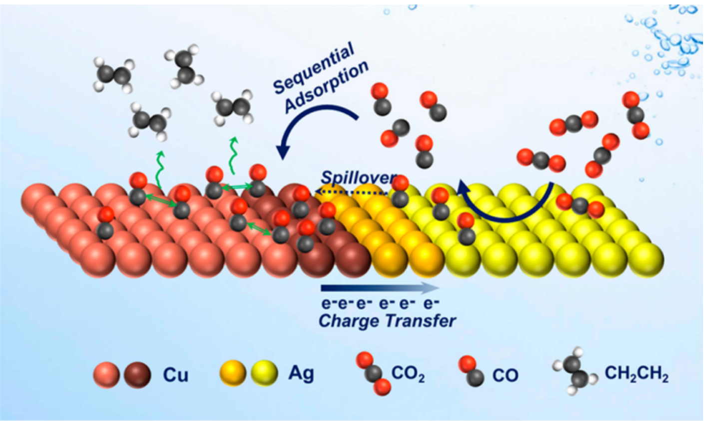

Figure 1.12: Tandem catalysis on Ag-Cu nanodimers (NDs) [41].

Zn-Cu bimetallic catalysts have been studied for two main benefits: the low activity of Zn for the HER [43, 44] and its lower cost compared to the other noble metals cited above.
Pt-Cu bimetallic catalysts show high CH_4 selectivity but the high activity for the HER have restricted their application [31].
Pd-Cu bimetallic catalysts lead to high CO and HCOOH selectivity [31, 45] but if used

in form of aerogel it becomes selective to methanol [46].

1.5 Ag-Cu bimetallic catalysts

As anticipated in the subsection 1.4.1, the objective is to provide a more detailed description about Ag-Cu bimetallic electrocatalysts with the aim of making clear the state of the art of this material and, in particular, the supposed working mechanism and its potentialities. First of all, it is important to say that Cu and Ag have very low miscibility between them [47], so most of these catalysts show phase segregated domains. In the literature several ways of coupling the two metals can be found and an attempt will be made to summarize the most relevant ones. Ag-Cu core-shell nanoparticles [48] show that, using an high coverage of Cu, the material owns greater hydrocarbons selectivity while, using a lower Cu coverage, an enhanced selectivity for CO is recorded. In order to isolate the tandem effect, Zhang and co-workers [49] have inserted a thin carbon interlayer between Ag core and Cu shell and it was found that the as prepared nanostructure produces high ratios of ethanol to ethylene by increasing the *CO coverage on the Cu surface. Additionally, using a porous Cu shell, it has been noted that the confinement of local CO concentration in the porosity increases the C-C coupling, resulting in 73% FE for C_{2+} products [50]. Another type of synergistic effect between Ag and Cu has been reported by Li et al. [51] synthetizing a series of Ag_xCu_{100-x} bimetallic catalysts by aqueous ice bath reduction to obtain high activity and selectivity for CO. The idea is to compensate for the shortcomings of both metals and in particular, the limited binding energies of Ag for *COOH and *CO that do not permit the achievement of high activity and selectivity for CO and the strong adsorption to *CO on Cu surface that can lead to CO poisoning. In tandem catalysts, the problem of not fully utilizing the CO produced by silver can be encountered and to solve it the Cu/Ag segmented GDEs (s-GDEs) has been proposed, in which the inlet CO-selective Ag catalyst layer (CL) extends the residence time of CO in the second C_{2+}-selective segment [52]. In the subsection 1.3.1 the Cu surface reconstruction phenomenon has been quoted with a negative connotation in terms of durability and activity but in a study on the AgCu nanoporous single atom alloy (SAA) catalyst [53] it was highlighted that this effect is used to achieve CO Faradaic efficiency of 97.5% taking advantage of the enhanced CO desorption. Another morphology has been presented by Dutta and co-workers [54], who prepared an AgCu metal foam activated towards alcohol through the application of a thermal annealing. This treatment allows the transformation of copper in its oxides (Cu_2O and CuO) leading to high durability (100h) and selectivity for ethanol (33.7%).

CHAPTER 2

Materials and methods

It is now intended to provide a presentation of all the operating methods adopted during the course of this experimental work. Beginning with a description of the procedure for synthesizing the bimetallic catalyst, the technologies used to conduct the electrochemical and material characterization will then be explained in detail.

2.1 Synthesis

The electrode preparation consists of two steps: (i) Cu sputtering deposition on carbon paper (GDL; SIGRACET 28BC, Ion power GmbH) in order to create GDE and (ii) Ag displacement, obtained by immersing Cu substrate in a Ag_2SO_4 (CAS: 10294-26-5, $\geq$99.99%, Sigma-Aldrich) aqueous solution, achieving in this way the final Ag-Cu bimetallic catalyst object of this study. The goal of the first step is to create a high surface area copper layer with a single deposition step, exploiting the same approach proposed by Monti and co-workers [55], which is advantageous because it enables good control of material properties as morphology and Cu loading. The employed device (Quorum Technologies Ltd., Q150T S) is based on a magnetron sputter target equipment (Figure2.1) in which plasma is confined near to the target thanks to a magnetic field. Ar^+ ions present in the plasma, through the collisions on negatively charged target material (Cu, 99.99%, Φ57 mm x 0.5 mm, Nanovision S.r.l.), eject target atoms which deposit on the substrate. Prior to the deposition, a preventive cleaning of the target is performed to avoid the presence of impurities that could compromise the material performance. This step is followed by the deposition onto the carbon paper by setting the applied current (50 mA) and the deposition time (400 s) as working parameters of the instrument. These input parameters have been chosen with the objective of achieving the best Cu thickness and mass loading, obtaining a GDE more selective to ethylene production but also with a good adhesion on carbon paper. The mass loading can be calculated as follows:

$$m_{\mathrm{Cu}}\left[\frac{\mu g}{cm^2}\right] = \frac{m_{\mathrm{Cu+GDL}} - m_{\mathrm{GDL}}}{A} \tag{2.1}$$

where:

- $m_{\mathrm{Cu+GDL}}$ is the final mass of GDE after Cu deposition $[\mu g]$,
- m_{GDL} is the initial mass of GDL $[\mu g]$,
- A represents the geometric area of the GDL substrate $[cm^2]$.

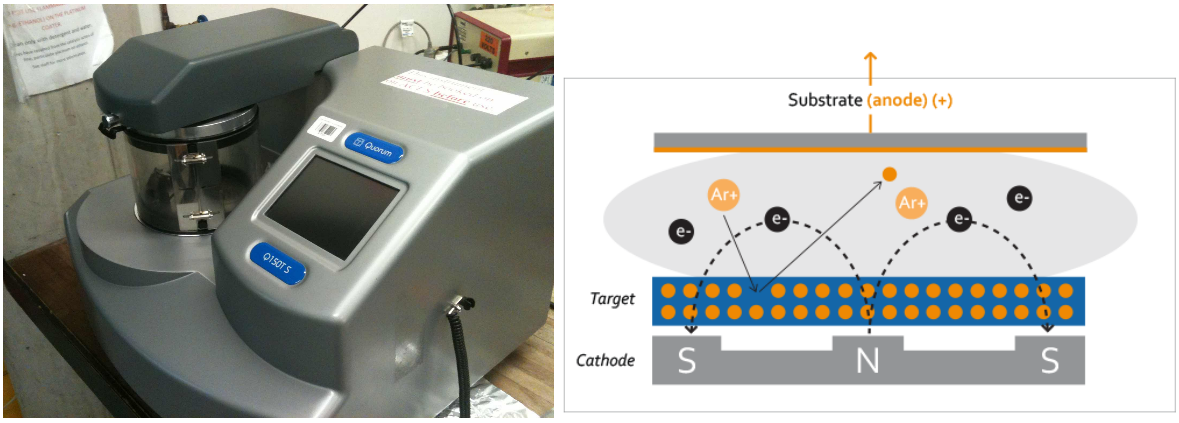

(a) Real experimental magnetron sputtering equipment [2]

(b) Schematic representation of magnetron sputtering operation [3]

Figure 2.1: Real (a) and schematic (b) illustration of magnetron sputtering apparatus.

The as prepared GDE is immediately subjected to immersion in silver salt solution to prevent surface air oxidation of copper. During this second step, two parameters of the solution have been modified to study how they affect the performance of the obtained electrode when it is used as the cathode in CO_2RR. In particular, different solution temperatures and immersion times have been employed. The experimental set-up is composed of three main components: (i) the hot plate stirrer, (ii) the heating water[4] bath and (iii) the silver salt aqueous bath. Fixing the plate temperature, the water/silicon oil in the biggest beaker is heated and consequently, the Ag_2SO_4 solution, placed in a small beaker (100 ml), reaches an homogeneous temperature throughout its volume, avoiding thermal gradients that could affect the final electrode compositional homogeneity (Figure2.2). The theoretical principle which rules the partial substitution between Cu atoms on GDE surface and Ag^+ ions present in the solution is based on

---

[2] `https://cmm.centre.uq.edu.au/quorum-q150t-metal-coater`

[3] `https://www.dentonvacuum.com/products/discovery/`

[4] Instead of water, silicon oil is used at high temperatures to avoid water evaporation, during this work only when a solution temperature of 90°C is required

the galvanic series according to which it exists a scale of nobility between dissimilar metals[56, 57]. In this case, the chemical reaction that happens is the following:

$$Cu + Ag_2SO_4 \rightarrow CuSO_4 + 2Ag \tag{2.2}$$

Silver is more noble than copper and for this reason, the first acts as the cathode and the Ag^+ ions reduce, and the second acts as the anode by oxidizing when they are immersed in an electrolyte (in this case water).

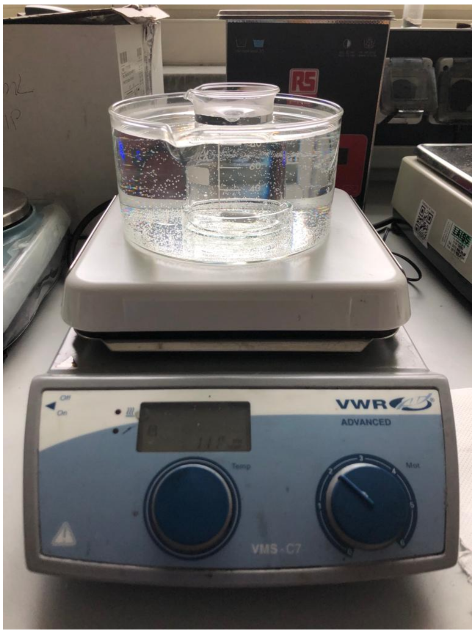

Figure 2.2: Experimental set-up adopted during Ag displacement process.

After extracting the electrode from the solution, a wash in deionized water and a drying using a laboratory compressed nitrogen blow gun are performed. Finally, the as obtained catalyst is stocked in the glove box (Labstar, Mbraun) to preserve the material from oxidation and contamination by taking advantage of the inert atmosphere (O_2, $H_2O < 1$ ppm).
In order to be submitted to the electrochemical measurement, the catalyst should be placed on the cathode plate that will be part of the cell device. The steps to be performed are as follows: (i) definition of the active area, (ii) creation of an electric contact between the metal plate and the catalyst using a copper tape and (iii) the covering of both sides of the plate (except the catalyst active area) with an insulating Teflon tape. The result is shown in Figure2.3.

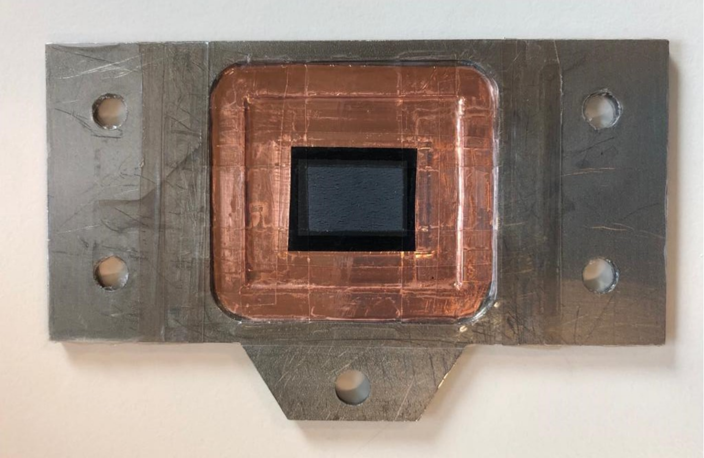

Figure 2.3: Catalyst on the cathode plate

2.2 Electrochemical characterization

The experimental electrolyzer set-up chosen for this work is a three-electrode cell in which the cathode (bimetallic Ag-Cu catalyst) is the working electrode and the anode (Ir-coated Ti plate, Ir-MMO, ElectroCell Europe A/S) is the counter electrode. Between cathode and membrane (anionic exchange membrane, Sustainion® 37-50, Dioxide materials) the reference electrode (Ag/AgCl, 3 M Cl^-, 1mm, leak-free LF-1) is inserted. The electrolyte chosen for this application is KOH (CAS: 1310-58-3, Sigma-Aldrich) 1 M aqueous solution because it reduces the HER even if it enables the salt formation, due to the reaction that occurs between it and the CO_2. The cell assembly starts with the creation of liquid anodic chamber, then the membrane is placed between two rigid plastic nets that avoid bubbles formation. Next, the liquid cathode chamber is created and the reference is inserted into it, as anticipated. At this point, the cathode plate can be placed, followed by the creation of the gas chamber, in which is insufflated CO_2, which laps the back of the cathode, triggering the reduction reactions (Figure2.4).

After preparing the cell, it can be placed inside the actual measuring apparatus by connecting the liquid (to both the anode and cathode) and the gas (cathode only) inlet and outlet tubes. It is important to specify that at the anode recirculation of the electrolyte is used to keep track of any CO_2 crossover phenomena that would vary the pH of the anolyte which must be similar to that of the catholyte (KOH 1M, pH=14), which otherwise exploits a single pass configuration. For all measurements performed, the liquid flux at the inlet is maintained, by using a peristaltic pump, at a value of 3.5 mL/min, while the gas flux is fixed at 25 mL/min thanks to the presence of a mass flow controller between the CO_2 tank and the gas inlet. Similarly, a mass flow reader is placed at the gas outlet pipe to check the outlet gas flow (hopefully as close as possible to the inlet gas flow) to keep track of any leaks in the device. Each electrode is then connected to the respective electrical terminal (white for reference, red for anode and

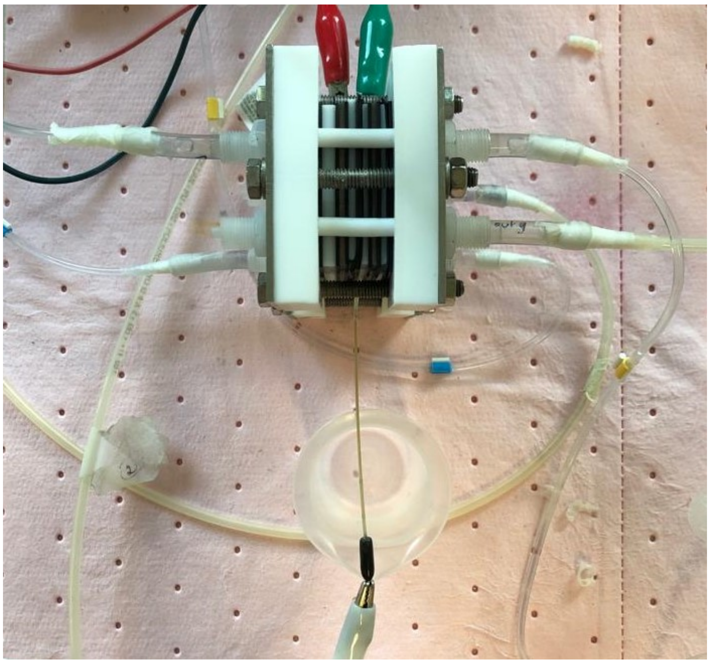

Figure 2.4: Real three-electrode cell apparatus

green for cathode). The illustration of the overall apparatus is shown in Figure2.5.

In the electrochemical characterization of the studied catalyst, three main instruments are involved. The analysis of liquid and gas products is carried out, respectively, in the HPLC (High-Performance Liquid Cromatograph, Nexera series, SHIMADZU) and in the μGC (Micro Gas Cromatograph, Fusion$^{®}$, INFICON). Finally, to perform the galvanostatic test a CH potentiostat (CHI760D) is used. Other informations on this equipment will be provided in the following sections.

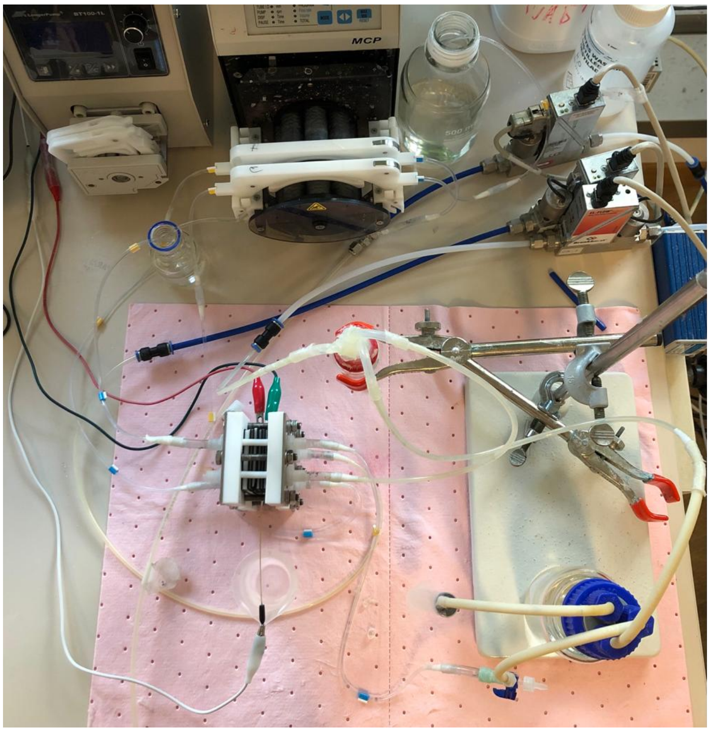

(a) Real experimental set-up

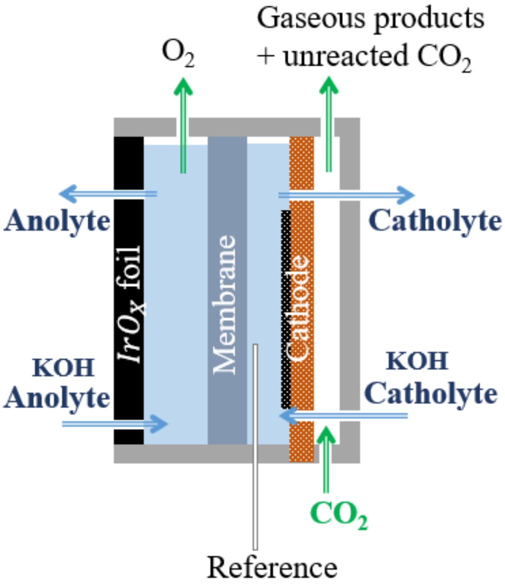

(b) Schematic representation of experimental set-up

Figure 2.5: Real (a) and corresponding schematic (b) illustration of entire experimental apparatus.

2.2.1 High Performance Liquid Cromatography

HPLC device takes care of the qualitative and quantitative analysis of the liquid products. In this study for each measure three liquid samples are collected from the cathode outlet: sampling after 120 s from the start of the measurement, sampling before the end of measurement (3600 s) and sample from the bottle in which is stored all the cathode liquid products. For the first two of these, it is appropiate to specify that sampling has a duration of 3 min. The last one is useful to get an idea of the average liquid feedstocks production and to understand whether or not it is stable during the time. Finally, a sampling from the anode bottle is collected to figure out if the crossover has occurred. The most important components of the HPLC instrument are the column (rm9.h0.s3008, Repromer H, 9 μm, 9 mM H_2SO_4, 300*8 mm, Dr. Maisch), the photodiode array detector (PDA) and the refractive index detector (RID). The column, to which a precolumn (rm9.h0.s0208, Repromer H, 9 μm, 20*8 mm, Dr. Maisch) is connected, has the task of separating the different liquid products. This is possible through the passage inside the column (stationary phase) of the mobile phase (sulfuric acid, 9 mM) into which, via a needle, the sample to be tested is injected. Depending on the strength of the interactions that are established between the functional groups (polar or apolar) located on the inner wall of the column and the ones located in the sample, the products exit the column at different instants of time defining characteristic retention times (tR) for each substance. The two detectors are concerned with providing quantitative information about the products estimating the concentration of the analytes. PDA is based on the physical principle that different materials absorb an electromagnetic wave at different wavelength and in addition, following Lambert Beer's law, the absorbance is proportional to the analyte concentration and for this reason can be used in order to perform a quantitative analysis. The set-up of this detector includes two lamps, a deuterium (190-380 nm) and a tungsten (380-800 nm) one to cover all the UV/visible range. The light emitted by the source impinge on the flow cell in which the sample is contained and all the different wavelengths are separated from a diffraction grating creating monochromatic rays that are detected by a photodiode that converts them in electrical signals. The rielaboration of these signals gives rise to chromatogram in which the intensity of signal in milli-Abosrbance Units (mAU) is plotted on the y axis with respect to the retention time in minutes (min) on the x axis (Figure2.6).

RID is based on light refraction. In particular, the flow cell is divided in reference (mobile phase) cell and sample cell. When visible light from tungsten lamp reachs the flow cell, if inside it there is the mobile phase only, refraction is not present but when there is the sample, the refractive index of light change and measuring this change through a photodiode, the chromatogram is constructed (Figure2.7) similarly to the

---

[5] `https://www.shimadzu.com/an/service-support/technical-support/analysis-basics/basic/absorbance_detector.html`

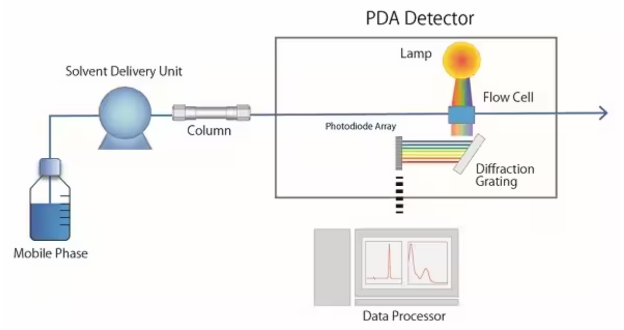

Figure 2.6: Schematic Diagram of a PDA detector [5]

PDA detector but using as unit for y axis milli-Volts (mV).

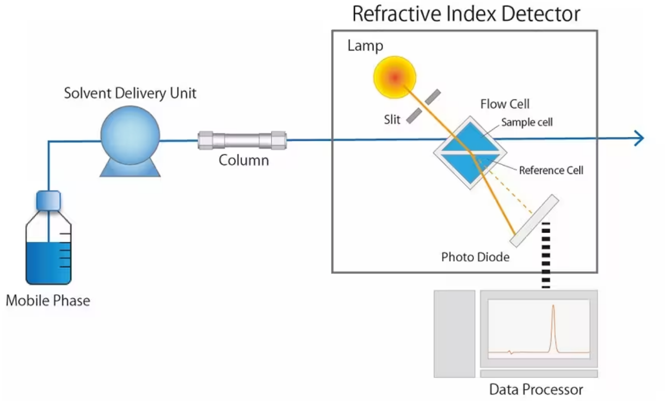

Figure 2.7: Schematic Diagram of a RID detector [6]

The typical liquid products that can be detected using HPLC device are: formic acid (HCOOH, tR = 9.4 s), acetic acid (CH_3COOH, tR = 10.19 s), ethanol (CH_3CH_2OH, tR = 14.2 s) and propanol ($CH_3CH_2CH_2OH$, tR = 15.9 s). After the data acquisition, it is possible to proceed with the liquids analysis integrating the peaks in correspondence of each specific substance retention time in order to obtain its concentration, useful to calculate liquid Faradaic efficiency, according to the following equation:

$$\%FE = \frac{V \cdot C \cdot n \cdot F \cdot \rho}{MM \cdot Q} \cdot 100 \tag{2.3}$$

where:

V is the sample volume [mL],

C is the product concentration [%v/v],

n is the number of electrons requerred for the reducing reaction [-],

---

[6] `https://www.shimadzu.com/an/service-support/technical-support/analysis-basics/basic/refractive_index_detection.html`

F represents the Faraday constant, 96485.3 C/mol,

ρ is the product density [g/mL],

MM represents the product molecular weight [g/mol],

Q is the electric charge [C].

2.2.2 Gas Chromatography

Adoperating a Micro Gas Chromatograph (Figure2.2.2), it is possible to perform the online gas analysis throughout the duration of the measure and, thanks to the presence of Fusion-Auto-Sensing Technology (FAST) and of MEMS (micro electro-mechanical system) μTCD (micro-thermal conductivity detector), reaches 1 ppm (parts per million) sensibility. It is important to specify that the instrument can be damaged from liquids and for this reason the gas outgoing from the cell, before being injected in GC device, is led in a "pre-chamber" so that, in case of flooding, there will be time to break the connection with the instrument before the liquid enters it. Similarly to what has been seen in HPLC for liquids, gaseous samples are injected along with the mobile phase into a column that allows the separation of the different compounds. In the specific case, there are two modules, A and B, the first uses Ar as mobile phase and deals with the separation of lighter molecules (CO, H_2, CH_4, N_2 and O_2), characterized by a retention time lower than CO_2. The second one deals with the separation of heavier gases (C_2H_4 and C_2H_6) and the mobile phase used is He. Separated gases arrive in the detector which works by detecting the difference in thermal conductivity between the reference (carrier gas) and the sample of interest, generating an electric signal and leading to the chromatogram construction. Compound concentrations can be traced by the area of the peaks in the chromatogram.

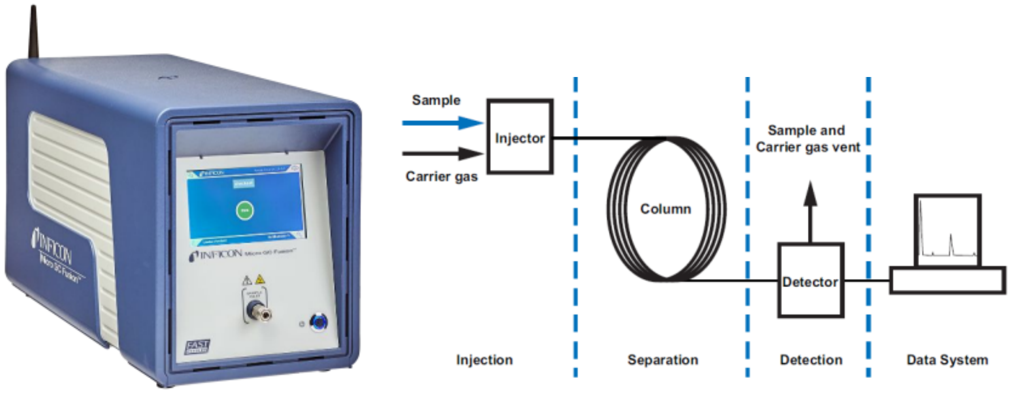

(a) Real experimental set-up (b) Schematization of GC working

Figure 2.8: Real (a) and corresponding schematic (b) illustration of GC device. [7]

Thanks to the extracted gases concentration, it is possible to calculate Faradaic efficiency for gaseous products using the following equation:

$$\%FE = \frac{\dot{V} \cdot C \cdot n \cdot F \cdot t}{V_m \cdot Q} \cdot 100 \tag{2.4}$$

where:

$\dot{V}$ is the flow rate of CO_2 at the cathode [L/min],

C is the product concentration [%v/v],

n is the number of electrons requerred for the reducing reaction [-],

F represents the Faraday constant, 96485.3 C/mol,

t is the time interval, fixed at 1 min,

V_m represents the molar volume for an ideal gas at standard temperature (0°C) and pressure (1 atm), 22.4 L/mol,

Q is the total electric charge passing through the cell during the measure in 1 min [C].

2.2.3 Galvanostatic test

The galvanostatic test is conducted through the use of an electrochemical workstation (CH potentiostat) which allows to set the parameters of the measurement. During this work, three different current densities (j) are used: 200, 400 and 600 mA/cm^2. It is possible to choose j by fixing the applied current during the measurement and by delimiting the electrode active area. The potentiostat is then responsible for keeping the current constant returning, as the output of the measurement, the trend of the potential as a function of time (Figure2.9).

It is essential to specify how it is determined the reduction potential represented on the y axis of the plot. First of all, it is necessary to introduce the equation that define V°, the electrode potential in standard conditions (1 atm, 298.15 K):

$$V^\circ = -\frac{\Delta G^\circ}{nF} \tag{2.5}$$

where:

ΔG° represents the standard Gibbs free energy of formation [J/mol],

n is the electrons involved in the rection [-],

F represents the Faraday constant, 96485.3 C/mol.

In not standard conditions, reduction potential V is calculated using the Nernst equation:

---

[7] `https://www.inficon.com/media/5744/download/Micro-GC-Fusion-Operating-Manual.pdf?v=1&inline=true&language=en`

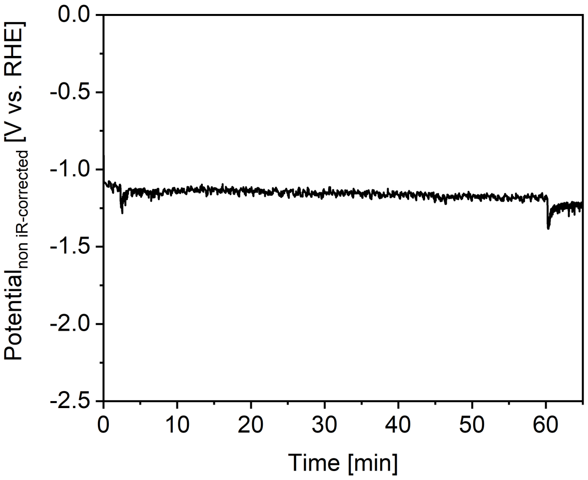

Figure 2.9: Typical obtained output from galvanostatic test.

$$V = V^{\circ} - \frac{RT}{nF} \ln \left(\prod_{i} C_i^{\nu_i} \right) \tag{2.6}$$

where:

R represents the ideal gas constant, 8.314 J/K· mol,

T is the absolute temperature, 298.15 K,

C_i is the concentration of the i-th species [M],

ν_i is the stoichiometric coefficient of the i-th species, which for reactants is taken with a negative sign, and vice versa for products [-].

This equation is used in this work in order not to neglect the influence of aqueous solution pH on the potential of the half reaction 2.7.

$$H^{+} + e^{-} \rightarrow \frac{1}{2} H_2 \tag{2.7}$$

In particular, the Nernst equation (2.6) applied to 2.7 becomes:

$$V = V^{\circ} + \frac{0.059}{n} \cdot pH \xrightarrow{V^{\circ}=0V, n=1} V_{RHE} = V_{SHE} + 0.059 \cdot pH \tag{2.8}$$

This transformation is a consequence of the regrouping of all the constants (R, T, F) and to the conversion factor between natural and base-ten logarithm (ln(x) = 2.3026·log(x)), remembering that pH is equal to -log[H^{+}]. At the as obtained potential another correction is applied in order to refer the potential to reversible hydrogen electrode (RHE), remembering that the reference used during the measurements is the Ag/AgCl electrode. Knowing the value of standard potential for the reference electrode ($V^{\circ} = 0.22$ V [58]) and applying the Equation 2.8, the electrode potential becomes:

$$\begin{aligned} &V_{applied}(vs.RHE) = V_{applied}(vs.Ag/AgCl) + V_{Ag/AgCl}(vs.SHE) + V_{SHE}(vs.RHE) \\ &V_{applied}(vs.RHE) = V_{applied}(vs.Ag/AgCl) + 0.22 + 0.059 \cdot pH \end{aligned} \tag{2.9}$$

Furthermore, it is appropiate to specify that during this study i-R correction of the potential, which takes into account the solution resistance due to the ion mobility in the catholyte, will not be applied. Nevertheless, before starting the measure and stopping it, resistance value is checked to ensure that it remains approximately constant during the time.

2.3 Materials characterization

To better understand the catalyst behavior during CO_2RR and find a connection between electrochemical performance and material properties, it is appropriate to conduct a morphological, compositional and structural characterization. The techniques adopted during this work are: Field Emission Scanning Electron Microscopy (FESEM, Supra 40, Zeiss, Oberkochen, Germany), Electron Dispersive Spectroscopy (Oxford EDS microanalysis, Liquid-N_2 cooled Si-Li detector) and X-Ray Diffraction (XRD, PANanalytical X'Pert Pro-diffractometer, Cu-Kα radiation, 40 kV, 40 mA, X'celerator detector). Some details on the instrumentation used and the principles of operation of the technique are given below.

2.3.1 Field Emission Scanning Electron Microscopy

Field Emission Scanning Electron Microscopy represents a very powerful technique for material characterization thanks to its higher achievable resolution (0.7-0.8 nm), magnification (20x-10^6x) and depth of field than common optical microscopy. All these advantages can be attributed to the energetic electron beam which acts as source and thanks to De Broglie rule 2.10 is possible to estimate the electrons wavelength ($\lambda_{DeBroglie} = 0.027$ nm if $E = 20$ kV) knowing their kinetic energy (E).

$$\lambda_{DeBroglie} = \frac{h}{p} \xrightarrow{E=\frac{p^2}{2m_e}} \frac{h}{\sqrt{2m_e E}} \tag{2.10}$$

where:

h is the Planck's constant, $6.626\cdot 10^{-34}$ J$\cdot$ s,

p is the electron momentum [kg$\cdot$ m/s],

m_e is the mass of one electron, $0.911\cdot 10^{-30}$ kg.

The electron beam generated at the top of the column by an electron gun based on field emission effect, was focused by magnetic lenses in the bottom chamber in which the sample holder is contained. The field emission effect is obtained thanks to a very sharp single crystal W tip. Applying a high potential between anodes and cathode (provided by W) a huge electrostatic field is created which, by tunnelling effect, can extract e- from the tip. The as extracted e- have brightness orders of magnitude higher than thermionic emission effect and for this reason the best resolution is achieved. Two sets of lenses shape the beam: the condenser and the objective. The first one controls demagnification of the beam confining it a cylinder using a ferromagnetic system while the objective focuses the beam on the sample surface in order to obtain the optimal focal length, thanks to the changing of magnetic field strength regulating the current inside the lens. Two sets of scan coils allow the raster scanning of the sample surface. The interaction between primary electrons (from the beam) and the target produce secondary electrons (SE), back scattered electrons (BSE), Auger electrons, X-ray photons, etc. Detecting all of them, it is possible to obtain a lot of information about material morphology and composition (Figure2.10).

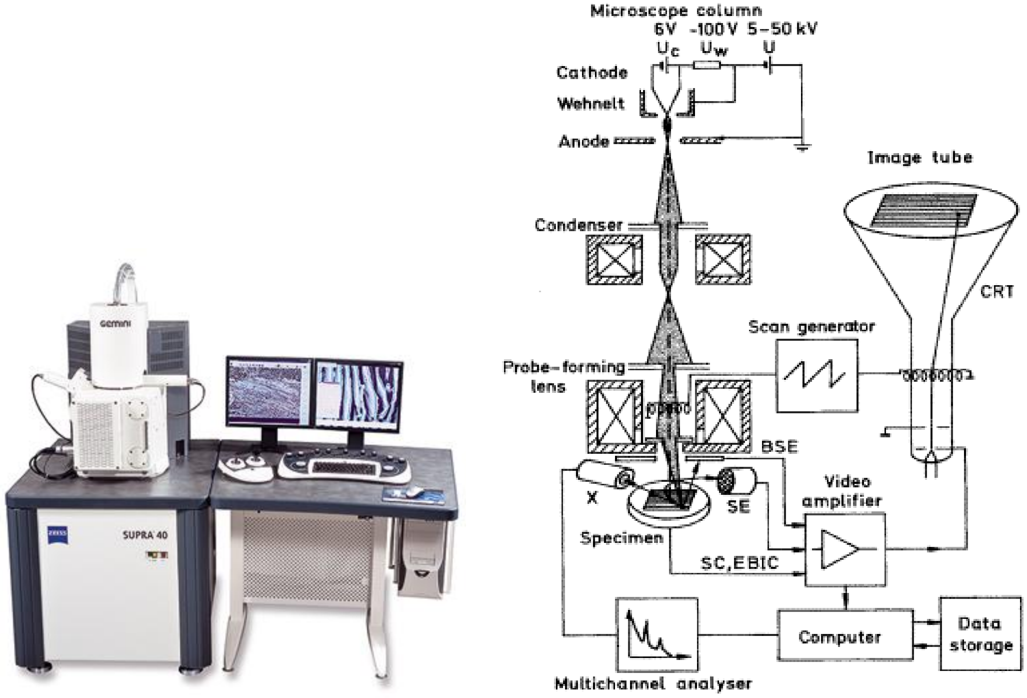

(a) Real experimental set-up[8] (b) Schematization of FESEM apparatus[9]

Figure 2.10: Real (a) and corresponding schematic (b) illustration of FESEM device.

Several kinds of detectors with different purposes can be present in FESEM set-up: Everhart-Thornley (E-T), Solid-state and In-lens devices are sensitive to SE and BSE.

---

[8] `https://speciation.net/Database/Instruments/Carl-Zeiss-AG/SUPRA-40-;i666`

[9] `https://inano.au.dk/research/research-platforms/nanoanalysis/transmission-and-scanning-electron-microscopy`

In particular, the first detector can be used for both SE (if it is applied a positive bias) and, more rarely, BSE (if it is applied a negative bias). The second one, is devoted to the detection of BSE while the last one is used only for SE. E-T system, through the presence of a scintillator material (CaF_2 doped with Europium), converts electrons in photons which are led into a photomultiplier (PMT). The photon flux is converted back to electron current at the first electrode of PMT, in which is created an electron cascade that is finally collected at the anode. Usually, In-lens detector in an E-T but in a different position. While E-T is collocated near to the sample surface with a tilting angle in order to optimize the detection of low energetic SE, the In-lens is putted on the top side of the objective lens and takes advantage of the acceleration of SE in order to obtain higher spatial resolution but losing the three-dimensionality of the image because of the absence of tilting. Solid-state detector can give information on both composition and topography thanks to the presence of four detector sectors and by adding the signals it is possible to have information on composition while, by subtracting signals it is obtained a topography image. In this study, morphological imaging is obtained through the use of In-lens detector.

2.3.2 Energy Dispersive Spectroscopy

Energy Dispersive Spectroscopy is a technique that can give qualitative and quantitative information on the material chemical composition. This kind of spectroscopy is based on the detection of X-ray photons emitted by the material when it is excited by an electron beam. For this reason, by adding a special detector inside FESEM apparatus it is possible perform it. In particular, materials are able to emit two different types of X-rays: characteristic and continuum (Bremsstrahlung) radiations, shown in Figure2.11. When the primary electron impinges on sample atom, can leave an electron vacancy in a core level of atom, due for instance to the creation of a SE. In order to compensate this vacancy, an outer electron decays releasing a quantity of energy equal to the difference of energy level between the outer and the inner electronic shell (keV), fitting the energy range of photons X. This characteristic X-ray photon represents the fingerprint of the element, and by collecting all of them it is possible to obtain several peaks in the EDX spectrum, each one corresponding to a different energy jump of electrons for the same chemical element. Continuum radiation can be interpreted as the background of the spectrum, due to the electrostatic repulsion between primary and sample electrons. The detector adopted is a p-i-n junction cooled at cryogenic temperature that works through the creation of electron-hole pairs when X-ray waves arrive on its surface. Detecting this electronic signal the spectrum (Intensity of signal-Energy of X-ray photon) is constructed. From the position on the x axis of the peak it is possible to understand the elements present in the sample (qualitative information) and from the height of the peak, the concentration of species can be estimated with a limit of detection (LOD) of 1 at.% (quantitative information).

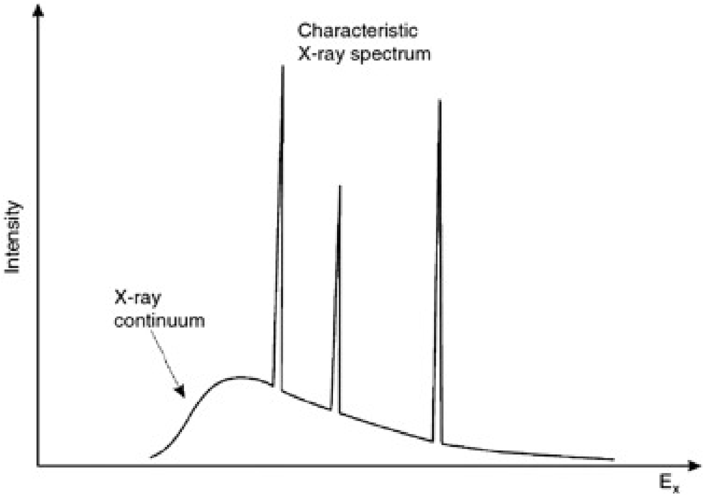

Figure 2.11: Typical EDX spectrum (Intensity of signal-Energy of X-ray photons)[59].

2.3.3 X-Ray diffraction analysis

X-Ray diffraction analysis is based on the Bragg's law:

$$n\lambda = 2d \sin\theta \tag{2.11}$$

where:

n is the order of diffraction, integer number (typically 1 or 2),

λ is the incident X-ray wavelength [nm],

d represents the interplanar distance [nm],

θ is the diffraction angle [degrees, °].
When the Equation 2.11 is satisfied, a family of crystalline planes (hkl) diffracts and it means that constructive interference occurs between electromagnetic waves because their wavelength is equal to their optical path difference ($2d\sin\theta$), as shown in Figure2.12.

In order to achieve this result, the diffractometer (Figure2.13) needs the presence of an X-ray source. In the Subsection 2.3.2 it has been explained that X-rays are generated when an electron beam impinge on a target which in XRD apparatus is a metal, for instance copper and as result, characteristic X-rays (K_α and K_β) are emitted by the metal target and directed on the sample.

So, if Bragg's law is satisfies, on XRD spectrum (Intensity-2θ) is possible to see a peak characteristic of a specific material crystalline plane.

---

[10] `https://cms.eas.ualberta.ca/xrd/how-xrd-works/`

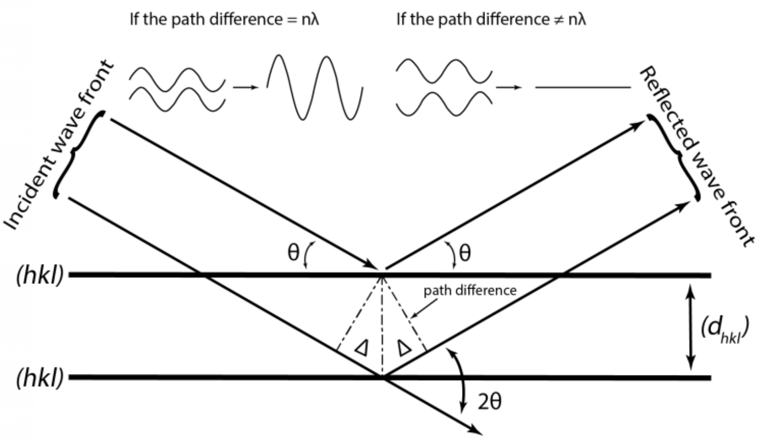

Figure 2.12: Schematic representation of X-ray diffraction^{10}

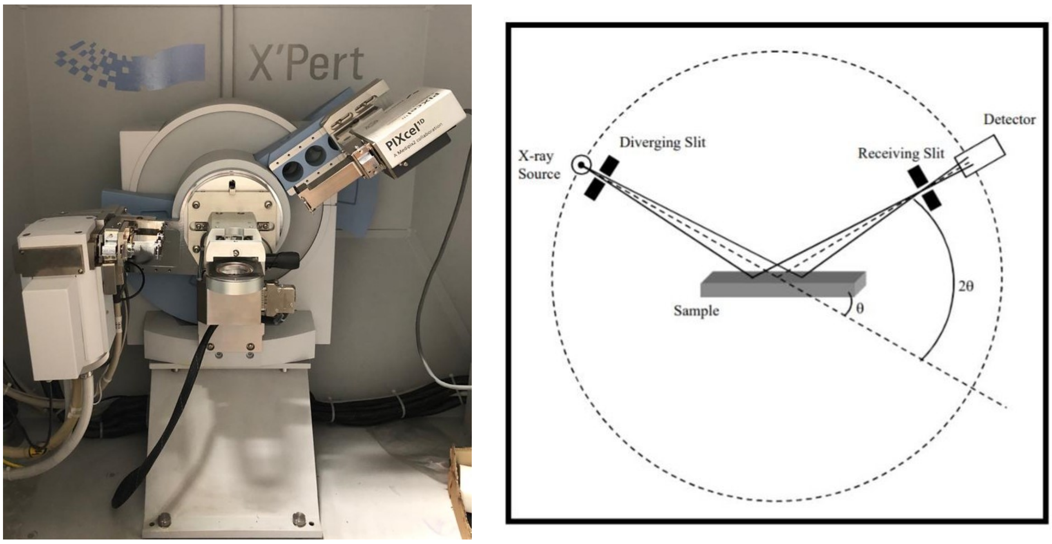

(a) Real XRD experimental set-up (b) Schematization of XRD apparatus[60]

Figure 2.13: Real (a) and corresponding schematic (b) illustration of XRD device.

Finally, thanks to tabulated reference XRD data for each crystalline material, it is possible to recognize crystalline phases present into an unknown sample by checking if all the peaks of the reference are present in the sample (Figure2.14) or determine the existence of a preferential orientation of the material comparing peak intensity (when peak intensity for a crystalline plane is higher than the corresponding peak in the reference spectrum, it means that the sample shows a preferential orientation in that crystallographic direction).

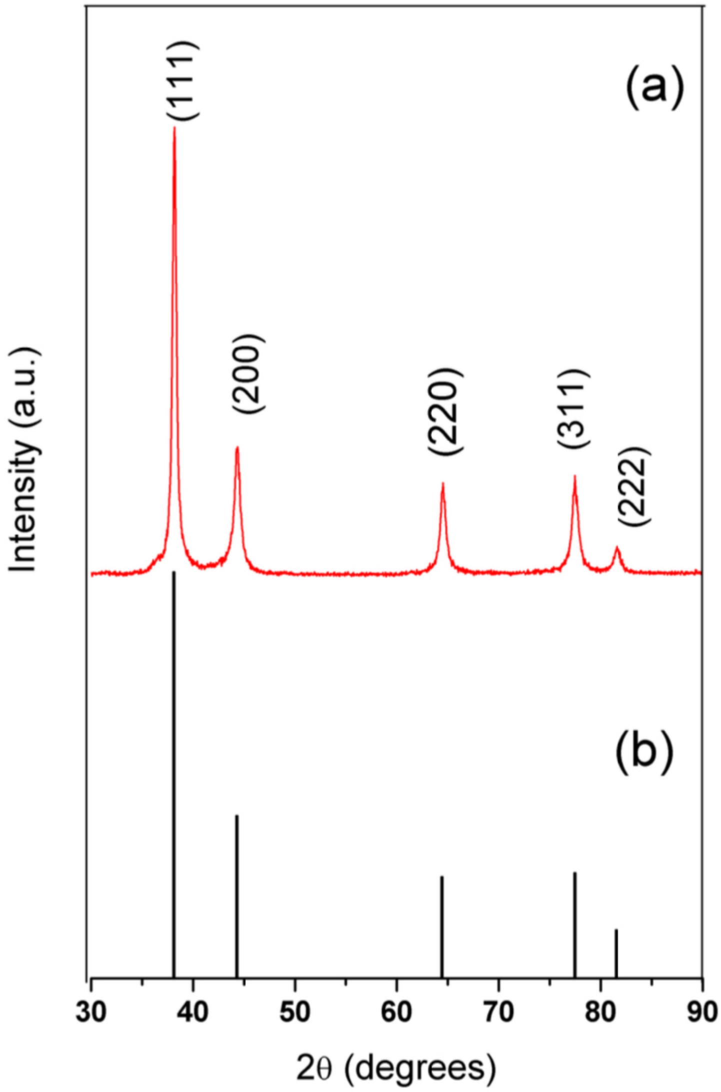

Figure 2.14: Example of XRD real spectrum (a) for Ag NPs and comparison with reference JCPDS file No. 04-0783 [61].

CHAPTER 3

Results and discussion

In this chapter are reported all the results obtained using the methods illustrated in the Chapter 2. First of all, a description of the study on different copper loadings will be provided. Subsequently, the investigation on the bimetallic catalysts will be carried out by dividing it according to the two synthesis parameters studied in this work: the solution temperature and the immersion time of the electrodes in the same. For each selected parameter, the electrochemical characterization accompanied by morphological and compositional analysis obtained by FESEM and EDS will be reported. While, at the end of the respective sections the XRD characterization will be illustrated along with comparisons between the different temperatures and immersion times chosen.

3.1 Copper loadings

As explained in Section 2.1, Cu GDEs are prepared using a magnetron sputtering fixing the deposition time at 400 s. The choice of this thickness is determined by the the screening of the samples obtained at different sputtering durations (50 s, 100 s, 200 s, 300 s, 400 s, 600 s, 800 s, 1000 s, 1200 s), which leads to the conclusion about what is the optimal synthesis parameter for this study. Calculating the Cu mass loadings (Equation 2.1) for each selected deposition time, it is possible to extrapolate the deposition rate from the slope of the straight line constructed from fitting the results obtained through calculations, by representing them on the y-axis as Cu loadings versus the deposition durations on the x-axis (Figura 3.1).

From the applied method it is found that copper is sputtered on GDL with a constant deposition rate of 0.34 μg cm^{-2} s^{-1}. Subsequently, subjecting all the samples to electrochemical characterization and calculating the Faradaic efficiencies for the gaseous products, it follows that increasing the sputtering time, the FE for C_2H_4 slightly increases until the deposition time of 400 s and then remains quasi-constant, as shown in Figure 3.2. Taking this result into consideration, it is decided to use 400 as the deposition time for all the bimetallic catalysts produced in this work, as a good trade-

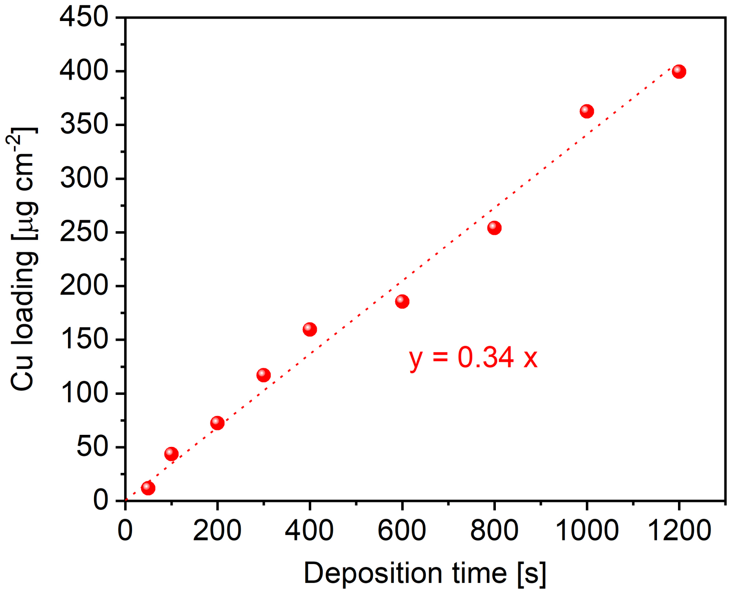

Figure 3.1: Linear correlation between Cu loading and deposition time.

off is obtained between selectivity for C_2 products and adhesion to the carbon paper, which is disadvantaged by excessive thicknesses.

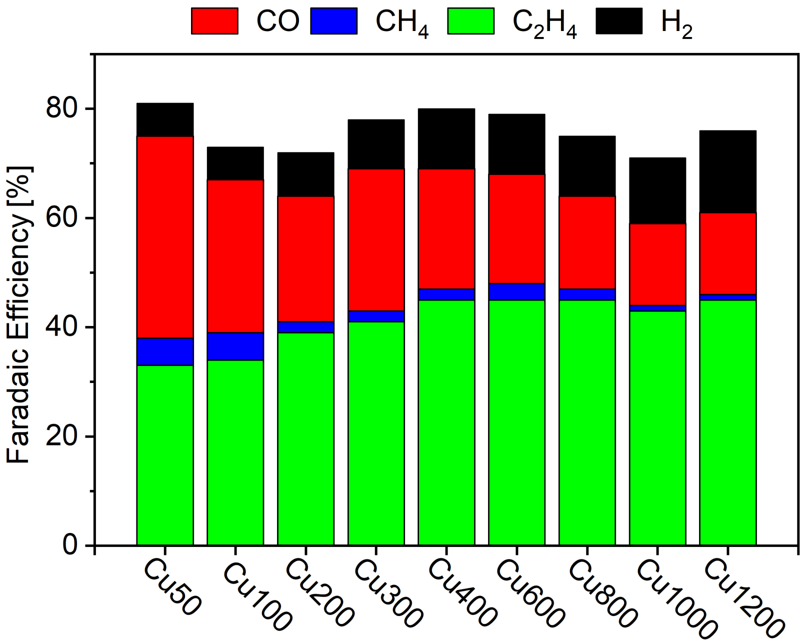

Figure 3.2: Comparison between the FEs towards gases for the different GDEs, tested in a flow cell with 1M KOH at -1.2 V vs RHE.

3.1.1 Cu 400 s

A detailed description of the electrochemical and morphological characterization of the electrode prepared using 400 s as deposition time (indicated as Cu 400 s) is now given. The **electrochemical characterization** is performed at three different current densities: 200, 400 and 600 mA cm^{-2}. The parameters of the galvanostatic tests are summarized in Table 3.1.

Table 3.1: Parameters of galvanostatic tests

Current density [mA cm^{-2}]	Current intensity [mA]	Active area [cm^{-2}]
200	300	1.5
400	200	0.5
600	300	0.5

Since the trends of potential (Figure 3.3a) and Faradaic efficiency for gaseous products (Figure3.3b) with respect to the time of measure (1 h) are, barring issues encountered during the tests (flooding, etc), all similar to each other, only the two respective plots for Cu 400 s tested at 400 mA cm^{-2} are given below. The latter are also to be considered representative for all other outputs of the potentiostat and GC, respectively, which are obtained from measurements made on the bimetallic catalyst.

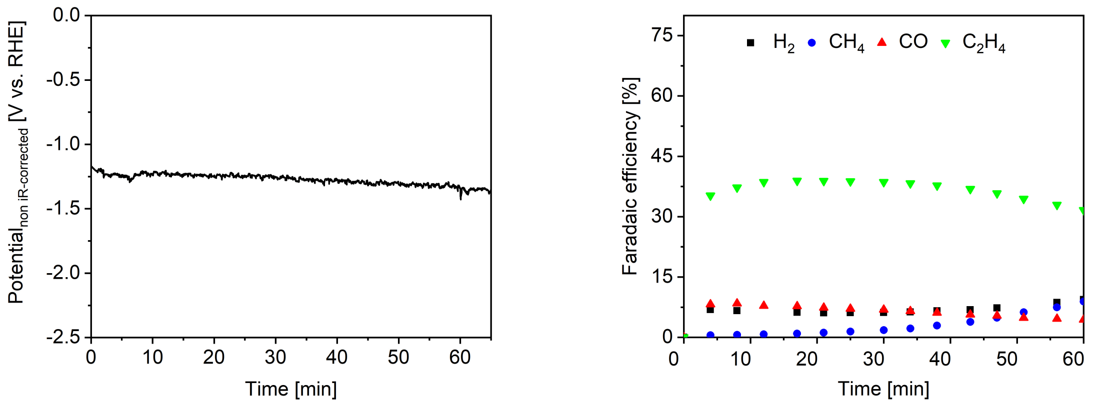

(a) Potential trend versus measure duration (b) FE for gases versus measure duration

Figure 3.3: Potential (a) and FE towards gases (b) with respect to the time.

During the measurement of the potential, it can be noted that in correspondence to the time intervals at which liquid sampling takes place (5-8 min for initial sampling, 60-65 min for final sampling), the potential undergoes a perturbation that manifests itself as a jump toward more negative values. This experimental observation is the basis for the decision to make the liquid sampling only at the beginning and end of the measurement so as to perturb it as little as possible and to allow the potential to remain at an almost constant value during the CO_2 reduction reactions. From the trend of Faradaic efficiencies for gaseous products during the test, it is possible to see good stability over time and that copper shows high selectivity toward ethylene. After making calculations of the Faradaic efficiencies for liquids as well, histograms are constructed, showing the total Faradaic efficiencies resulting from the sum of the liquid and gaseous chemicals collected at the different current densities studied (Figure3.4a). A comparison in terms of production of C_2 feedstocks (ethylene, ethanol and acetic acid) is shown in Figure3.4b. There is an increase in ethanol and acetic acid production and a slight decrease in selectivity toward ethylene at higher currents. Maximum C_2 production is reached at 400 mA cm^{-2} for Cu 400 s.

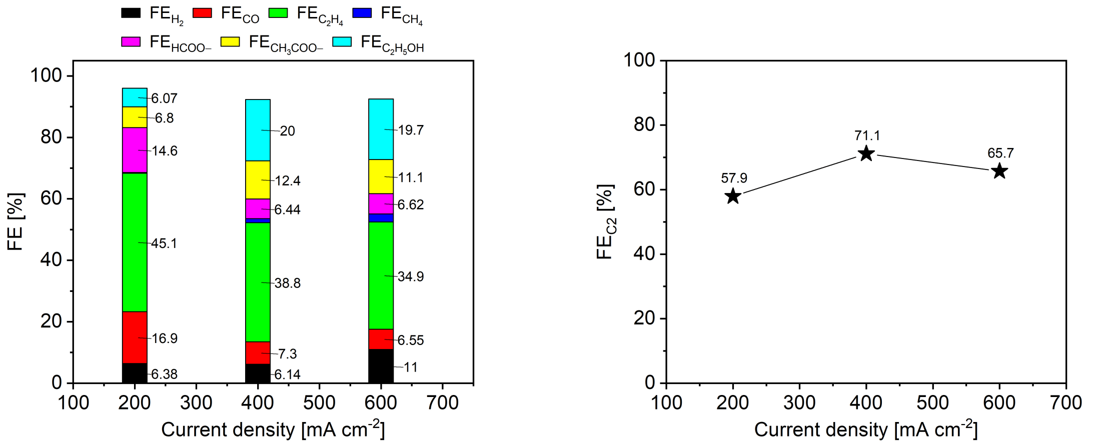

(a) Total FE at different current densities

(b) FE for C_2 products over current density

Figure 3.4: FE for all detected products (a) and C_2 products (b) for Cu 400 s at different current densities.

Material characterization of Cu 400 s is performed with FESEM. In particular, the morphological analysis is referred to Inlens detector using increasing magnifications (Figure 3.5). From the micrographs, it is possible understand how the growth of the thin layer of spattered copper on the GDL is organized structurally. Copper NPs are observed, generating nano-clusters that are in turn organized into nano-domains. The surface conformation appears to exhibit also high micro-roughness and porosity, suggesting an high specific surface area.

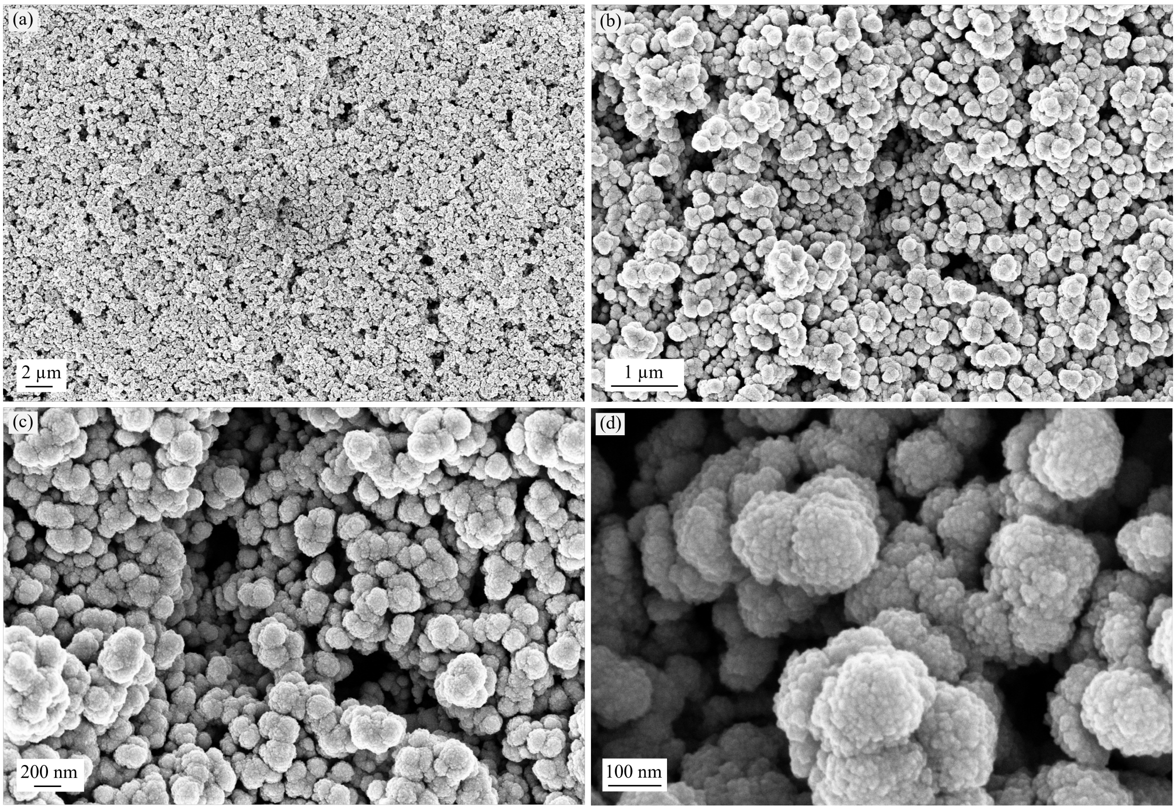

Figure 3.5: FESEM images of Cu 400 s at different magnifications: (a) 5K; (b) 25K; (c) 50K and (d) 200K.

3.2 Cu-Ag catalysts: different solution T

In this Section starts the discussion on the synthesized Cu-Ag bimetallic catalysts, beginning with the characterization of the materials prepared by fixing the immersion time (5 min) and concentration of the solution (0.5 mM), and varying its temperature (T). In particular, four different T are studied (25, 50, 75 and 90°C) and the macroscopic view of these samples together with Cu 400 s is represented in Figure3.6. Each sample is tested at three different current densities (Table 3.1).

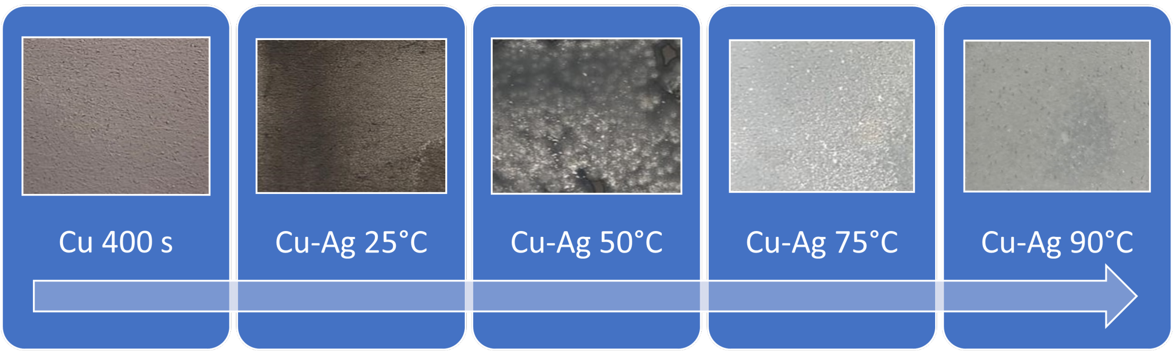

Figure 3.6: Macroscopic view of Cu-Ag 25/50/75/90°C and Cu 400 s.

3.2.1 Cu-Ag, 25°C

The **electrochemical characterization**, following the same scheme presented for Cu 400 s in Subsection 3.1.1, returns the results shown in Figure 3.7.

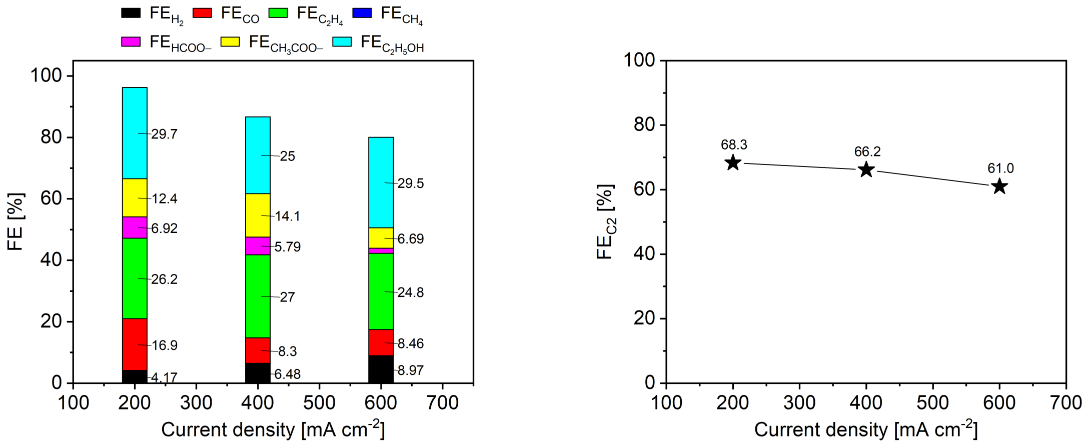

(a) Total FE at different current densities

(b) FE for C_2 products over current density

Figure 3.7: FE for all detected products (a) and C_2 products (b) for Cu-Ag 25°C at different current densities.

Compared with pure copper, ethylene production drop while ethanol production rise. The best performances are observed at 200 mA cm^{-2}. **Material characterization** is carried out through the use of FESEM and EDS. The images obtained from the Inlens detector are reported in Figure 3.8. From the micrographs, is possible to see clearly the presence of Ag on Cu clusters and it is also glaring that the distribution of silver plates on copper is not homogeneous over the whole surface. Applying EDX technique to a sample area (Figure 3.9a), the compositional spectrum (Figure 3.9b) of the analyzed surface is derived, from which it is possible to figure out which elements are present and their amounts in atomic percentages (Table 3.2).

Table 3.2: Composition of Cu-Ag 25°C

Element	Atomic %
C K	68.32
O K	8.48
F K	6.60
Cu L	14.57
Ag L	2.02
Total	100.00

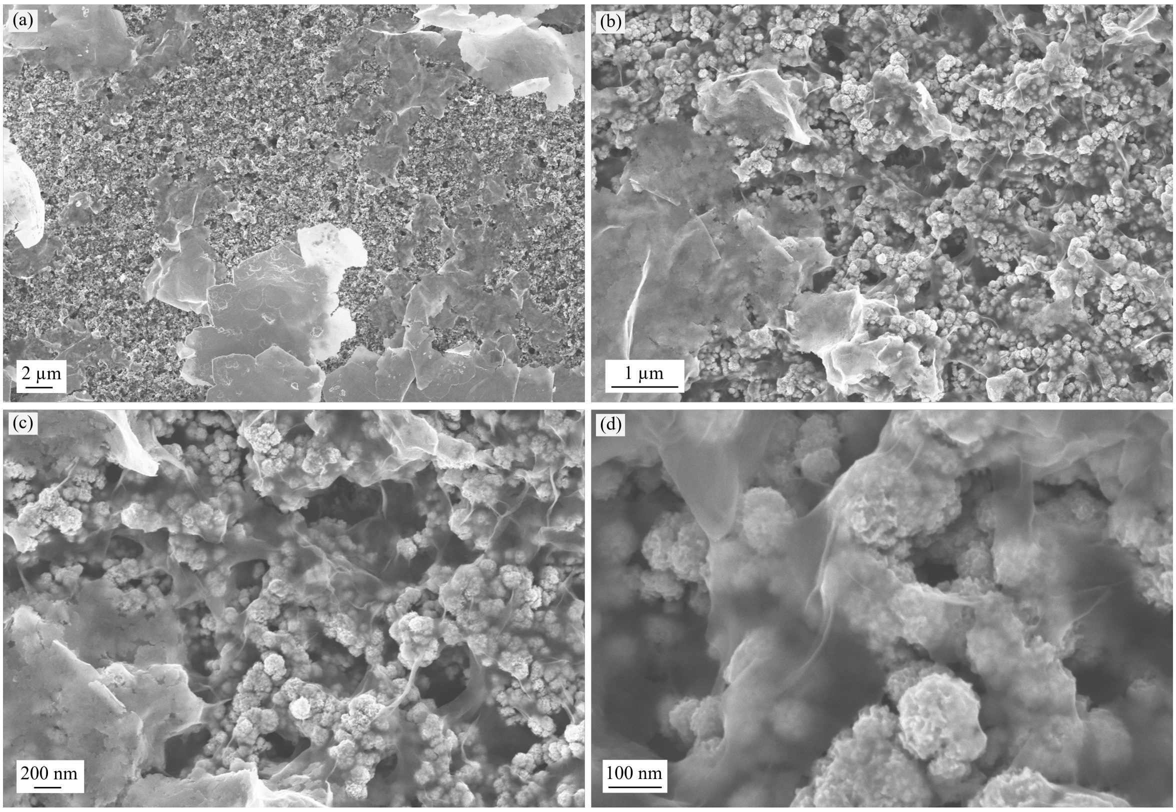

Figure 3.8: FESEM images of Cu-Ag 25°C at different magnifications: (a) 5K; (b) 25K; (c) 50K and (d) 200K.

Excluding C, O, and F deriving from carbon paper, dust and other contaminants, only Ag and Cu at.% are considered in order to estimate Ag/Cu ratio and how it is correlated with synthesis parameters. For Cu-Ag 25°C this ratio is equal to 0.14.

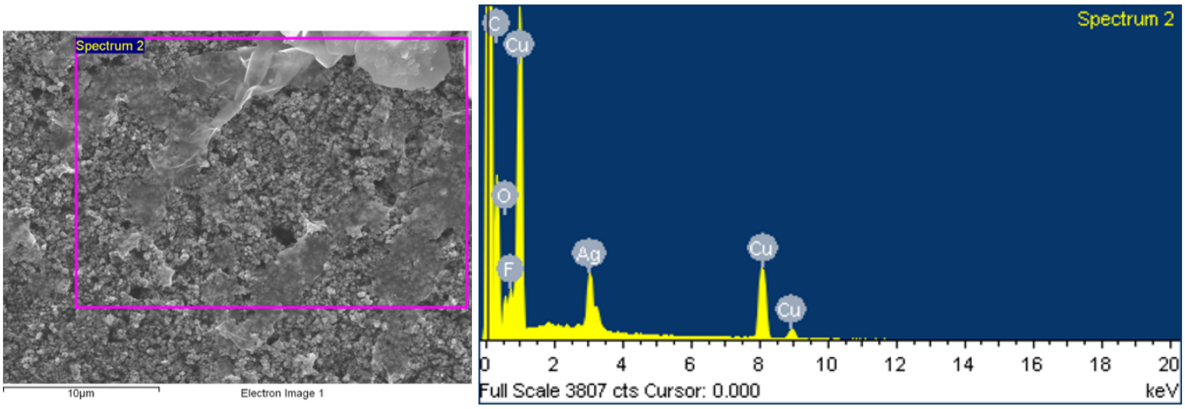

(a) Area defined for EDX scanning (b) EDX spectrum

Figure 3.9: Sample area (a) and corresponding EDX spectrum (b) for Cu-Ag 25°C.

3.2.2 Cu-Ag, 50°C

The analysis of the products generated during CO_2RR for the catalyst synthesized with a solution temperature of 50°C (Cu-Ag 50°C) is shown in Figure 3.10. FE for C_2 compounds reaches the maximum value at 200 mA cm^{-2}, as for the previous sample although the selectivity towards ethylene increases compared to Cu-Ag 25°C.

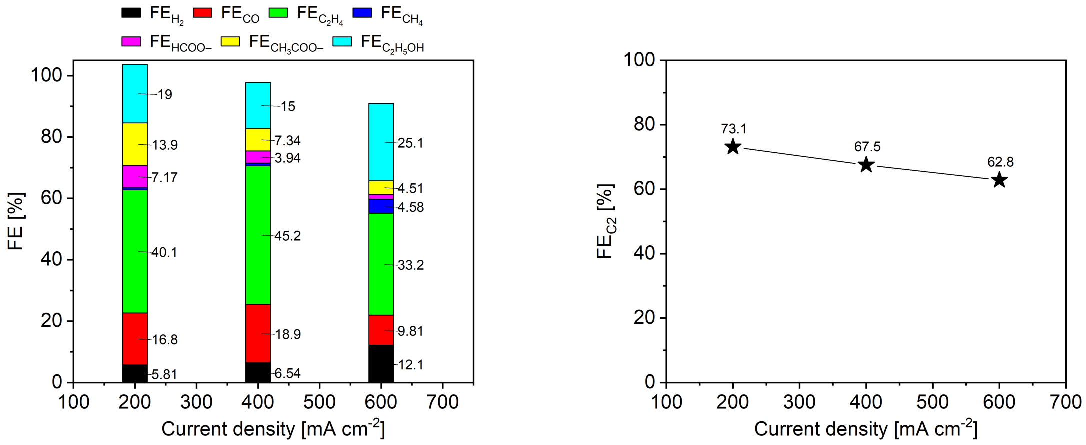

(a) Total FE at different current densities (b) FE for C_2 products over current density

Figure 3.10: FE for all detected products (a) and C_2 products (b) for Cu-Ag 50°C at different current densities.

The characterization of the electrode with FESEM (Figure 3.11) reveals interesting information. From the image captured at lower magnification (5K), the presence of silver flakes seems to be more uniform on the Cu substrate, that is still visible. Ag arrangement does not follow a specific orientation but it is possible to visualize aggregates deposited on the Cu layer in different directions (parallel, perpendicular, etc.) with respect to the substrate. Another new detail to note is the presence of some nanostructures grown on top of the silver plates. During the description of XRD analysis this topic will be taken up again. Finally, through the EDS (Figure 3.12) is possible to find the composition for this material (Table 3.3) and calculate the Ag/Cu ratio, which in this case is 0.26. For this material and others, small percentages of sulfur are found to be present, probably due to the silver sulfate solution.

Table 3.3: Composition of Cu-Ag 50°C

Element	Atomic %
C K	37.04
O K	30.30
S K	0.55
Cu L	25.49
Ag L	6.62
Total	100.00

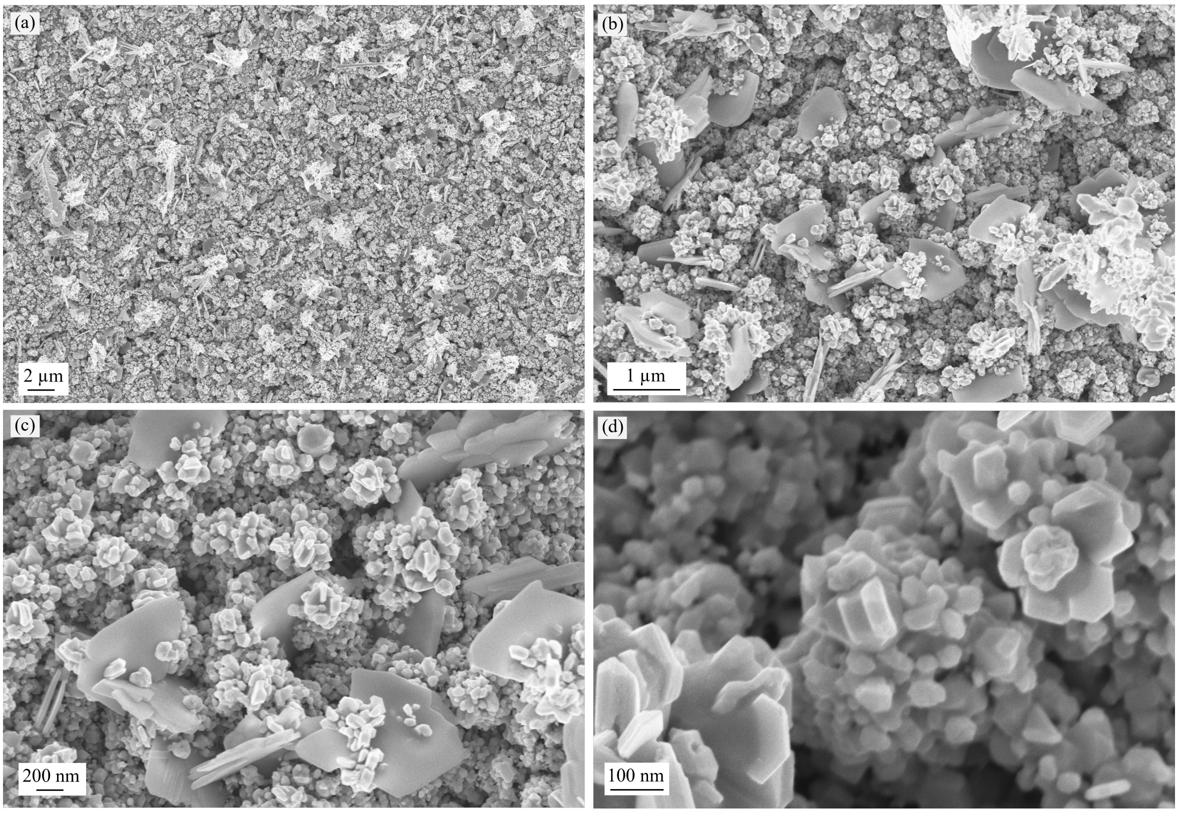

Figure 3.11: FESEM images of Cu-Ag 50°C at different magnifications: (a) 5K; (b) 25K; (c) 50K and (d) 200K.

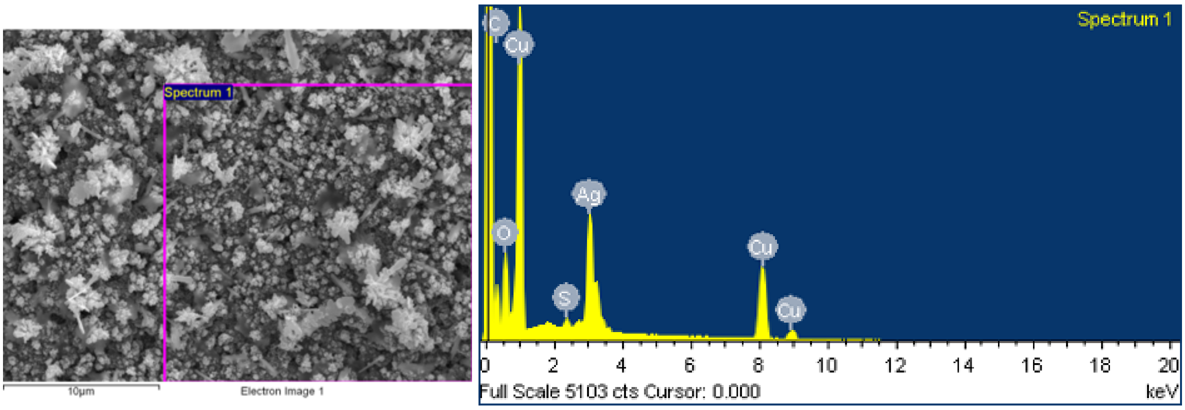

(a) Area defined for EDX scanning (b) EDX spectrum

Figure 3.12: Sample area (a) and corresponding EDX spectrum (b) for Cu-Ag 50°C.

3.2.3 Cu-Ag, 75°C

The electrocatalytic performances of the electrode Cu-Ag 75°C are summarized in Figure 3.13. Comparing it with previous ones, this electrode seems to keep unchanged performance even at high current densities.

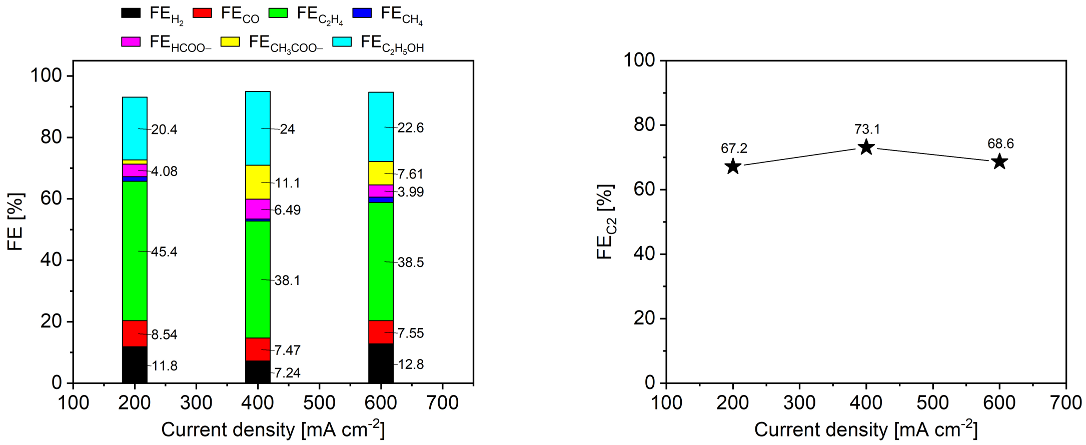

(a) Total FE at different current densities (b) FE for C_2 products over current density

Figure 3.13: FE for all detected products (a) and C_2 products (b) for Cu-Ag 75°C at different current densities.

With regard to FESEM micrographs (Figure 3.14), the topography of the examined material looks very different to the previous one (Cu-Ag 50°C): the Cu layer is completely covered by Ag and no longer visible at every magnification and the high nanostructurization present in previous samples seems to be lost. One hypothesis is that the copper, driven by the increase in synthesis temperature, tends to restructure itself in micro-domains. EDS reveals the elemental composition (Figure 3.15, Table

3.4) and allows calculation of an ever-increasing value for the Ag/Cu ratio, which in this case results in 0.7.

Table 3.4: Composition of Cu-Ag 75°C

Element	Atomic %
C K	9.33
O K	59.12
S K	2.77
Cu L	16.95
Ag L	11.83
Total	100.00

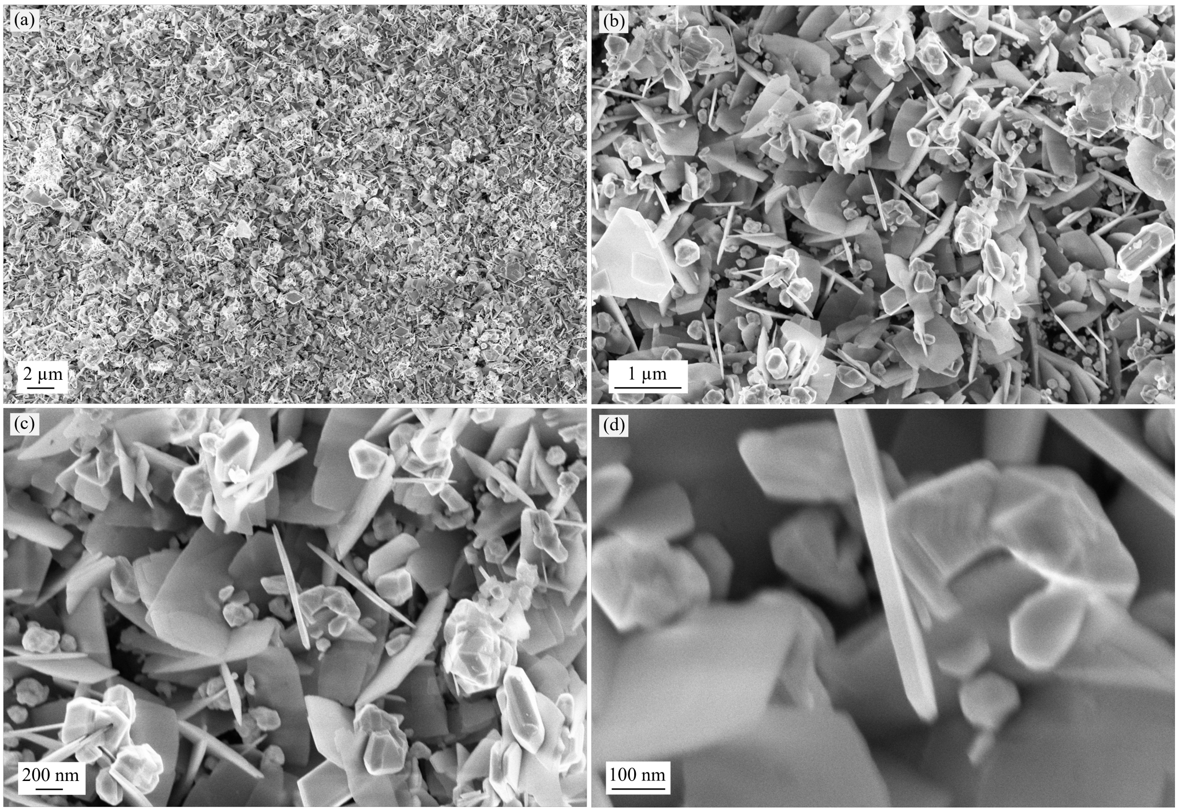

Figure 3.14: FESEM images of Cu-Ag 75°C at different magnifications: (a) 5K; (b) 25K; (c) 50K and (d) 200K.

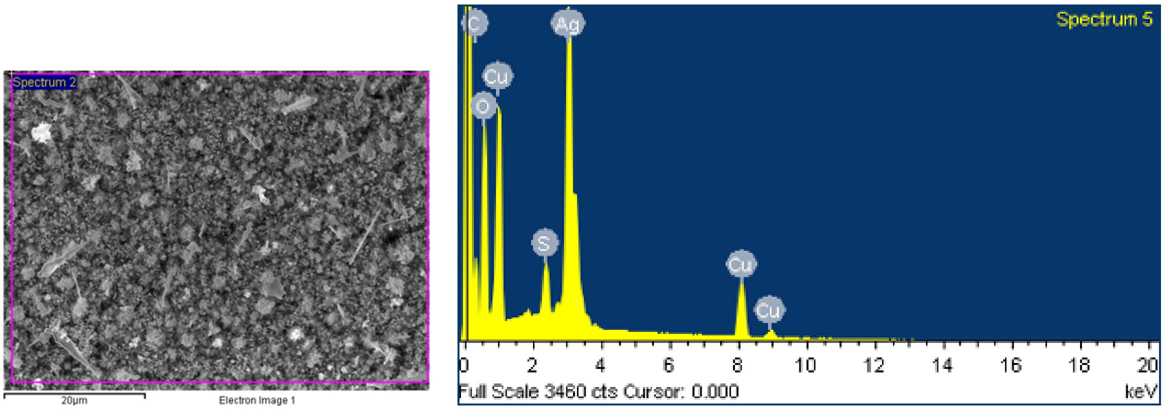

(a) Area defined for EDX scanning

(b) EDX spectrum

Figure 3.15: Sample area (a) and corresponding EDX spectrum (b) for Cu-Ag 75°C.

3.2.4 Cu-Ag, 90°C

The bimetallic catalyst prepared with a solution temperature of 90°C (Cu-Ag 90°C) shows the following electrochemical features during CO_2RR.

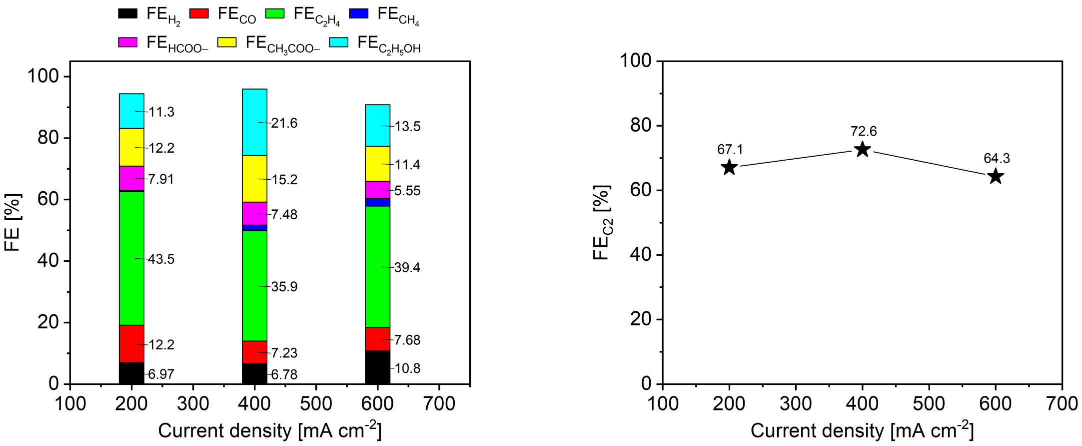

(a) Total FE at different current densities

(b) FE for C_2 products over current density

Figure 3.16: FE for all detected products (a) and C_2 products (b) for Cu-Ag 90°C at different current densities.

Compared to the sample Cu-Ag 75°C, FE for the products of interest does not shows high improvements and this justifies the choice of conducting the study on the influence of different immersion times on the electrode synthesized at 75°C, as it allows for high performance with less energy consumption during the production of the material. FESEM analysis confirms the morphology of the Cu-Ag 75°C catalyst by giving, at high magnifications (200K), a clearer view of the structure of the Cu/Ag[11]-based aggregates,

---

[11] From the EDX analysis only, it is not possible to identify with certainty the particle composition

that appear to grow on the edges of the silver flakes, taking on a characteristic C-shape (Figure 3.17). EDS outputs are shown in Figure 3.18 and in Table 3.5. Ag/Cu ratio is equal to 0.8.

Table 3.5: Composition of Cu-Ag 90°C

Element	Atomic %
C K	23.97
O K	51.77
S K	1.96
Cu L	12.39
Ag L	9.91
Total	100.00

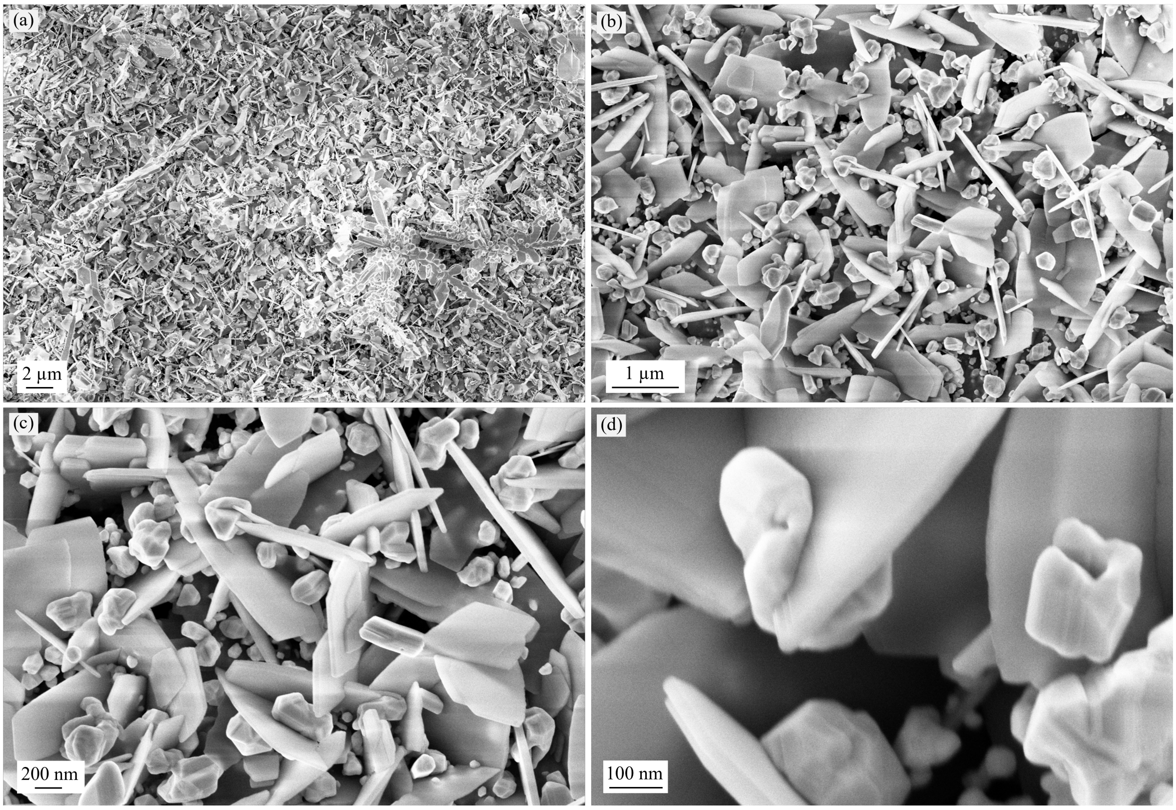

Figure 3.17: FESEM images of Cu-Ag 90°C at different magnifications: (a) 5K; (b) 25K; (c) 50K and (d) 200K.

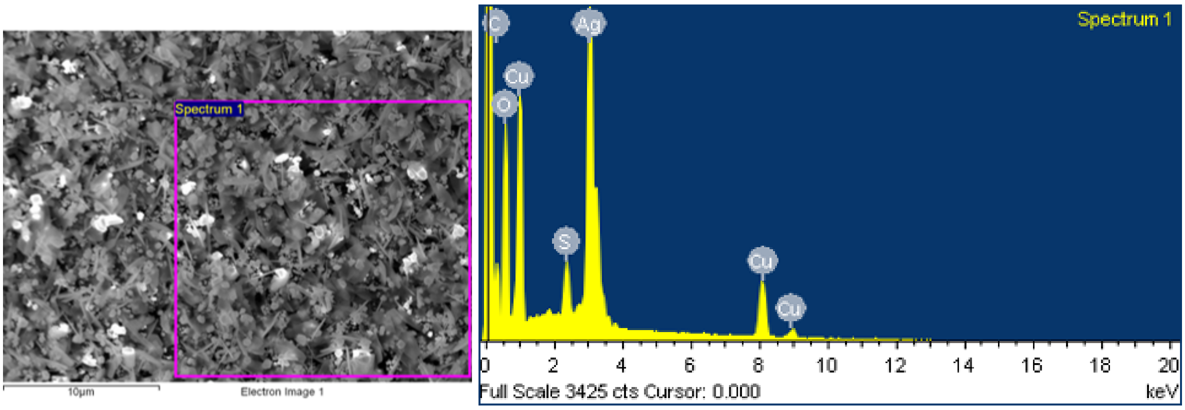

(a) Area defined for EDX scanning

(b) EDX spectrum

Figure 3.18: Sample area (a) and corresponding EDX spectrum (b) for Cu-Ag 90°C.

3.2.5 XRD analysis

XRD analysis results are now provided. The spectra of GDL and Cu 400 s are added to the four characteristic spectra of each temperature studied to make some additional comparisons (Figure 3.19). In order to identify the crystalline phases present in the analyzed sample, the obtained spectra has been compared with the reference data sheets of Ag (00-004-0783), Cu (00-004-0836), Cu_2O (00-005-0667) and Ag_3O_4 (00-040-1054). The first datum to observe is that the spectrum for the sputtered copper sample is identical to the one of the carbon paper substrate. Probably the thickness of the copper is so low that this type of analysis is not possible, and in fact the only peaks present are those of the GDL. For the first bimetallic produced through the immersion in the solution at 25°C is observed one Ag peak at $2\theta=38^\circ$. As the temperature increases, the Ag/Cu ratio increases and the appearance of silver peaks in the diffraction spectrum increase both in intensity and in number. The presence of copper and silver oxides is probably caused by air exposure of the sample during transport to the analysis laboratory and also during the performance of the XRD test itself, being in a non-controlled atmosphere (inert or vacuum). Very interesting and unexpected is the presence of copper oxide since theoretically the bimetallic material studied should be constituted only by the Cu layer (not visible through this kind of test) and by the Ag obtained from the galvanic displacement. It can be supposed a sort of re-deposition of Cu on Ag and maybe this phenomenon could be linked to the Ag/Cu aggregates found with FESEM (3.2.4). Another hypothesis that could explain the presence of these bigger particles made of Ag, Cu or both of them, is that maybe the electrode becomes unstable at higher solution temperature (above 50°C) and the Cu reconstructs itself in these big particles before the Ag displacement takes place. Other considerations on this topic will be made in the Chapter 4.

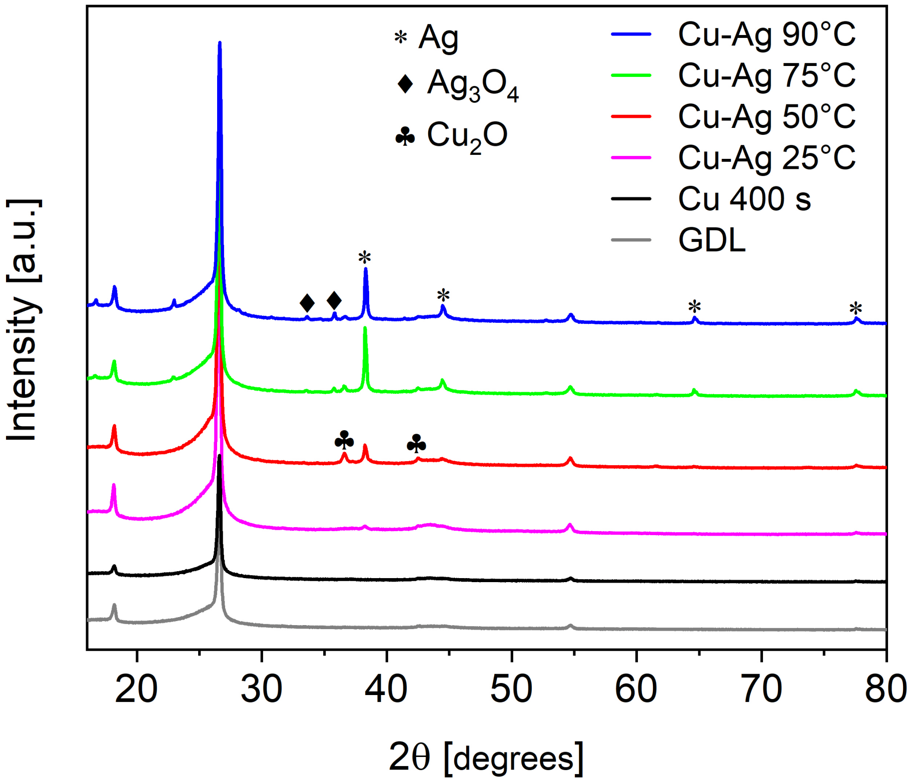

Figure 3.19: XRD spectra for GDL, Cu 400 s and the four bimetallic catalysts synthesized at different T.

3.2.6 Comparisons

In this concluding subsection, some comparisons of synthesized electrodes with different solution temperatures are presented. At the level of elemental composition, the influence of temperature manifests itself as an increase in the Ag/Cu ratio, as shown in the graph in Figure 3.20.

The greatest increase in this parameter occurs when the temperature is increased from 50 to 75°C. This observation is in agreement with what has been said about the micrographs of these electrodes, in which the samples Cu-Ag 75°C and 90°C show greater Ag coverage than the remaining two examined cathodes. It is deemed appropriate, given the amount of data collected in this study, to show a comparative graph (Figure 3.21) of the electrochemical performance of the four electrodes at the different current densities.

In comparison with pure copper, it can be seen that all bimetallic catalysts show higher C_2 production when tested at the minimum current density. This result is very important because it means that more high value-added feedstocks are obtained (with

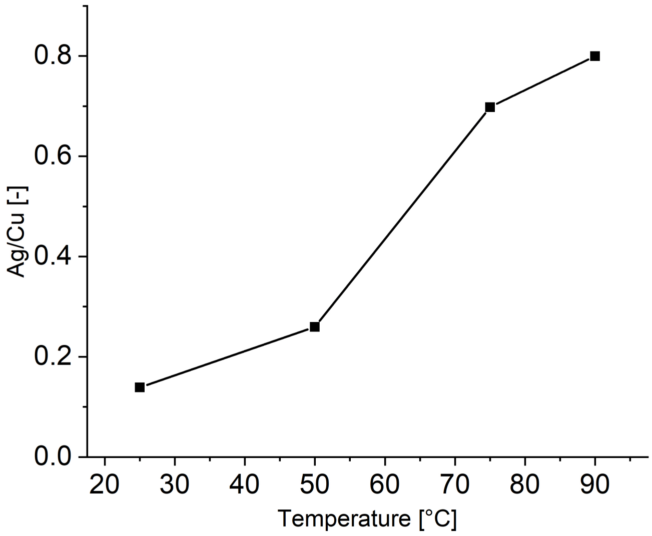

Figure 3.20: Ag/Cu ratio trend with respect to different solution temperatures.

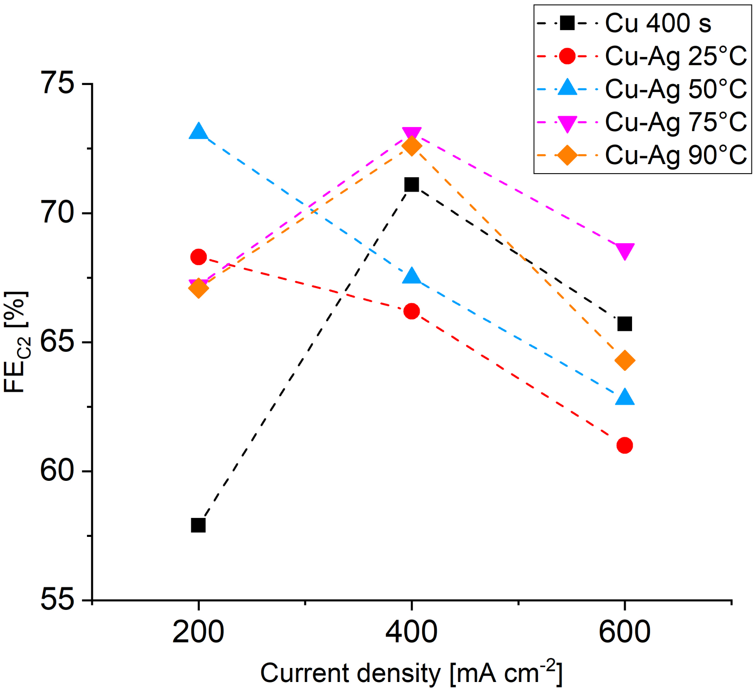

Figure 3.21: Comparison between FE to C_2 products for Cu 400s and Cu-Ag 25/50/75/90°C over current density.

an increase in FE of about 10-15%) by providing less current for the development of reduction reactions. It is also possible to distinguish two characteristic trends: Cu 400 s and Cu-Ag 25/50°C maximize the performance at 400 mA cm^{-2} while Cu-Ag

75/90°C, as current density increases, manifest a decrease in C_2 generation.

3.3 Cu-Ag catalysts: different immersion times

The second kind of study conducted on the bimetallic material, as anticipated, has the aim to investigate the influence of the time of immersion during the performing of Ag displacement on the electrocatalytic and structural cathode properties. In particular, solution temperature is fixed at 75°C (3.2.3) and in this case, for each electrode only one galvanostatic test at the current density of 200 mA cm^{-2} is carried out. The solution concentration is always equal to 0.5 mM. In addition to the sample synthesized using an immersion time of 5 min described above, two other dipping durations are studied: **1 min** and **3 min**. The three catalysts are indicated as Cu-Ag 1 min, Cu-Ag 3 min and Cu-Ag 5 min from now on (Figure 3.22).

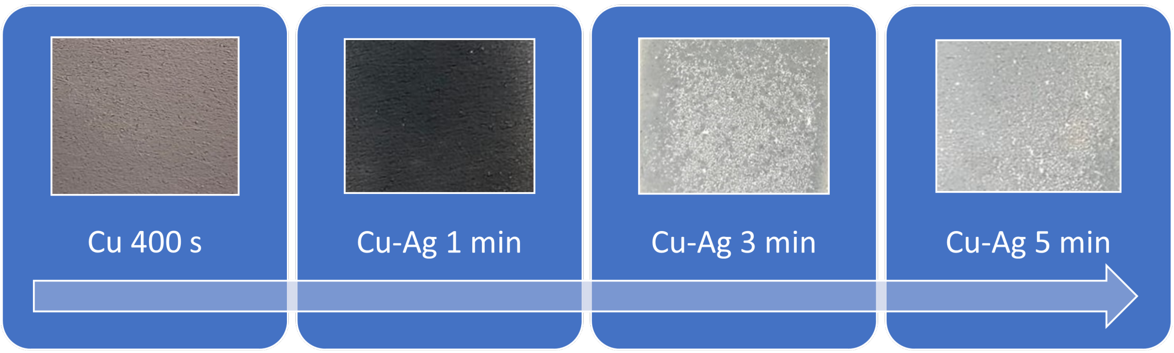

Figure 3.22: Macroscopic view of Cu-Ag 1/3/5 min and Cu 400 s.

The results of **electrochemical characterization** are illustrated in Figure 3.23a as the total FE and in Figure 3.23b as the FE to C_2 achieved by the three catalysts with respect to the immersion time, since the current density is constant. In terms of multi-carbon production, Cu-Ag 1 min and Cu-Ag 3 min show approximately the same selectivity (around 65%) and a slight improvement is obtained increasing the immersion time at 5 min. Anyway, the presence of silver allows a significant rise in the production of ethanol in comparison with Cu 400 s, as is possible to see in Figure 3.24 in which copper layer is positioned at the immersion time value of 0 min, and this leads to higher C_2 activity for the examined bimetallic cathodes.

Morphological (Figures 3.25, 3.27) and compositional (Figures 3.26, 3.28; Tables 3.6, 3.7) analysis is given only for Cu-Ag 1 min/3 min since in Subsection 3.2.3 the **material characterization** for Cu-Ag 5 min has already been submitted.

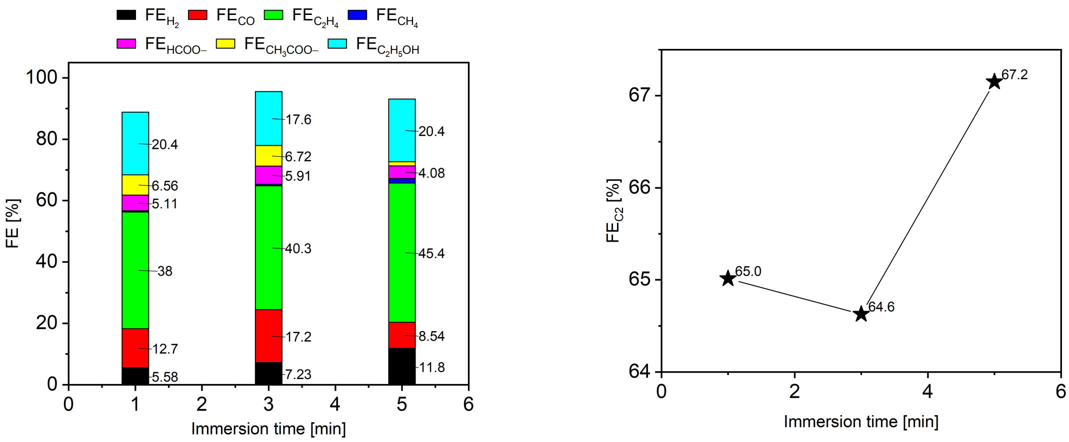

(a) Total FE at different immersion times (b) FE for C_2 products over immersion time

Figure 3.23: FE for all detected products (a) and C_2 products (b) for Cu-Ag 75°C tested at 200 mA cm^{-2} at different immersion times.

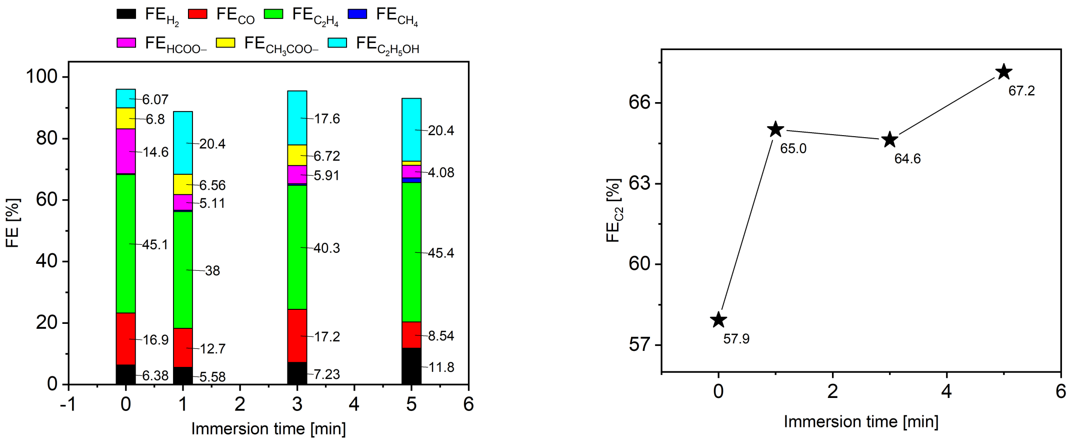

(a) Total FE at different immersion times (b) FE for C_2 products over immersion time

Figure 3.24: FE for all detected products (a) and C_2 products (b) for Cu-Ag 75°C 200 mA cm^{-2} at different immersion times versus Cu 400 s.

Table 3.6: Cu-Ag 1 min composition

Element	Atomic %
C K	52.67
O K	16.72
F K	4.82
S K	0.00
Cu L	21.92
Ag L	3.87
Total	100.00

Table 3.7: Cu-Ag 3 min composition

Element	Atomic %
C K	28.56
O K	42.17
F K	6.01
S K	1.71
Cu L	11.69
Ag L	9.85
Total	100.00

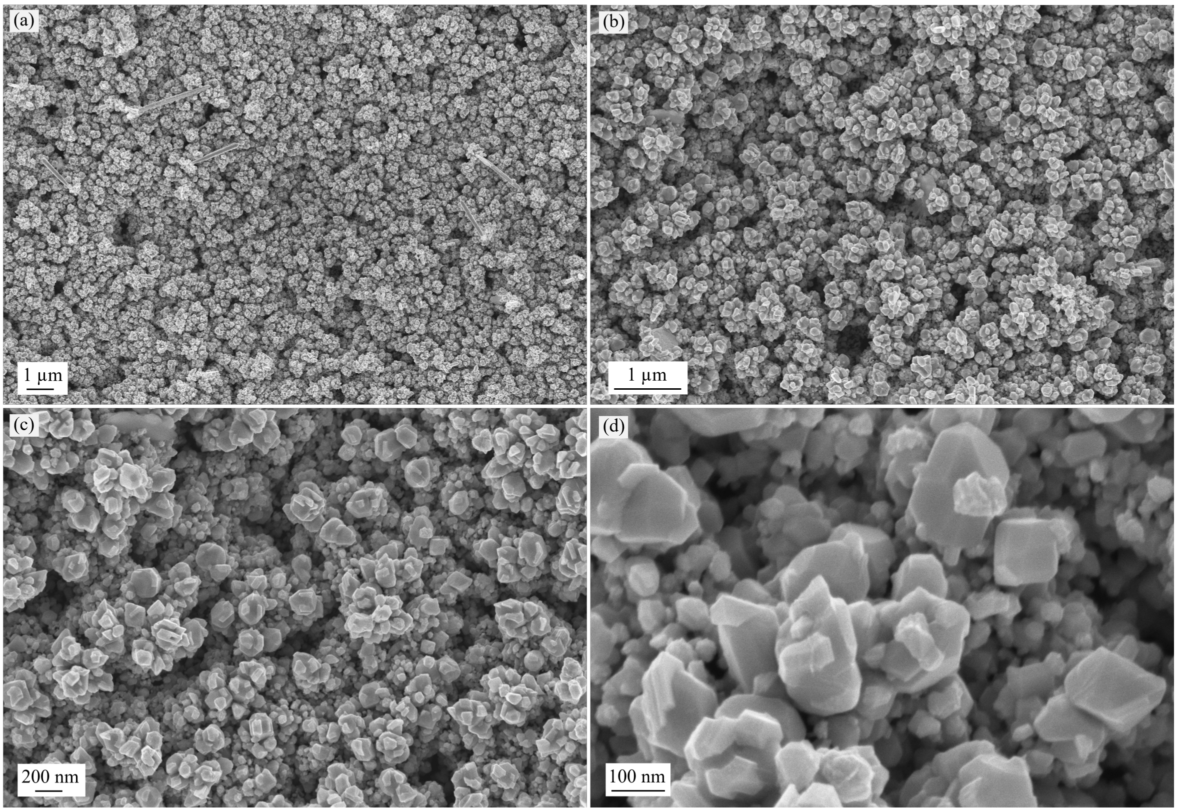

Figure 3.25: FESEM images of Cu-Ag 1 min at different magnifications: (a) 10K; (b) 25K; (c) 50K and (d) 200K.

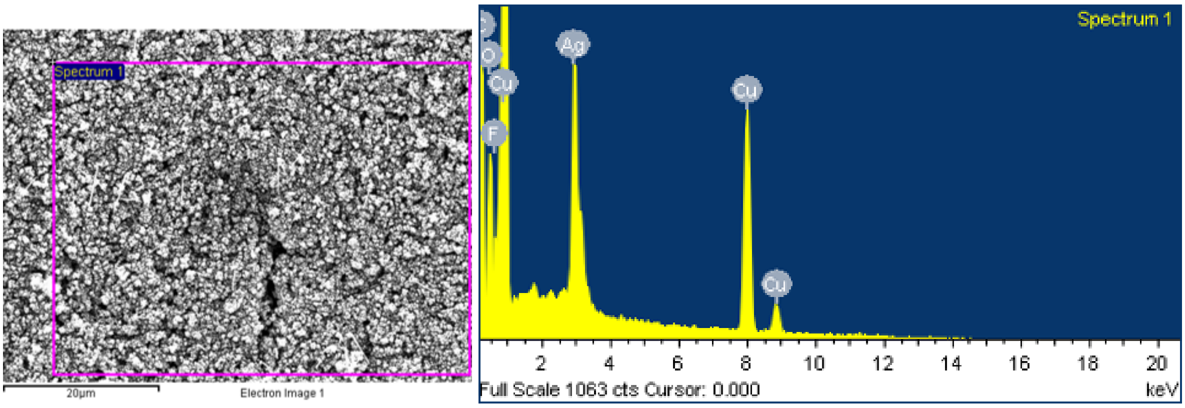

(a) Area defined for EDX scanning

(b) EDX spectrum

Figure 3.26: Sample area (a) and corresponding EDX spectrum (b) for Cu-Ag 1 min.

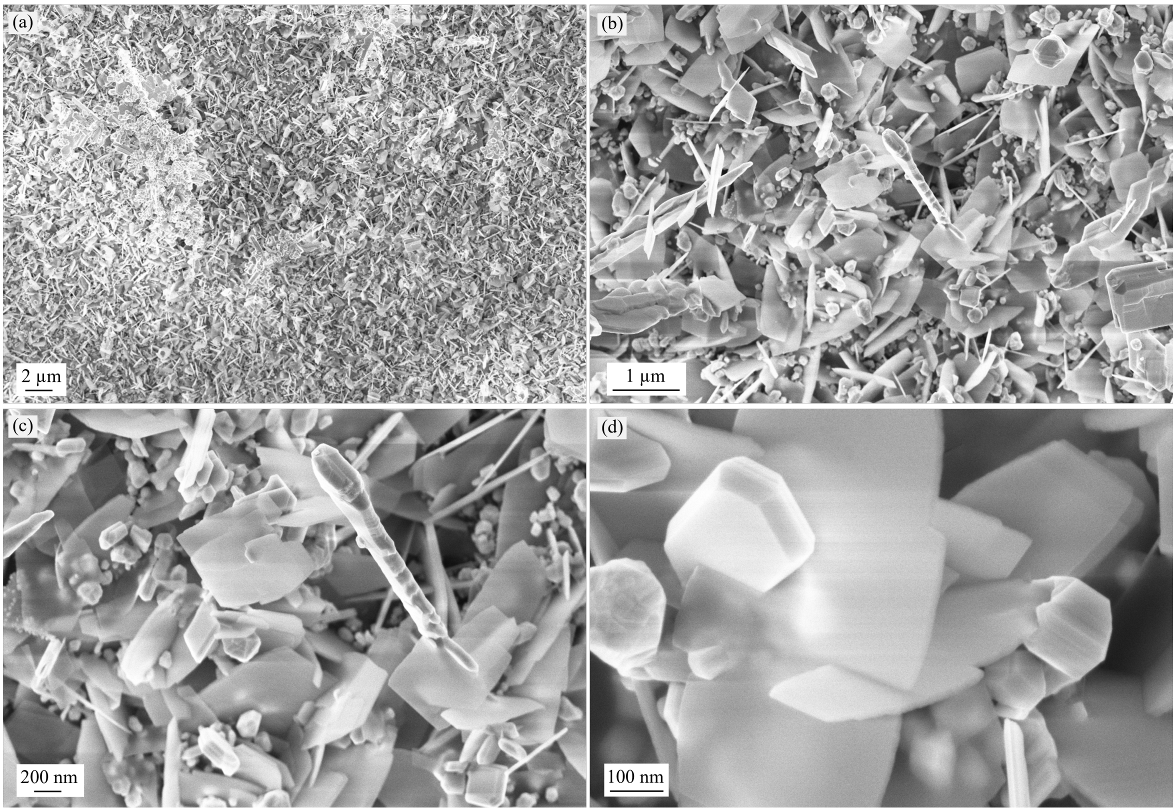

Figure 3.27: FESEM images of Cu-Ag 3 min at different magnifications: (a) 5K; (b) 25K; (c) 50K and (d) 200K.

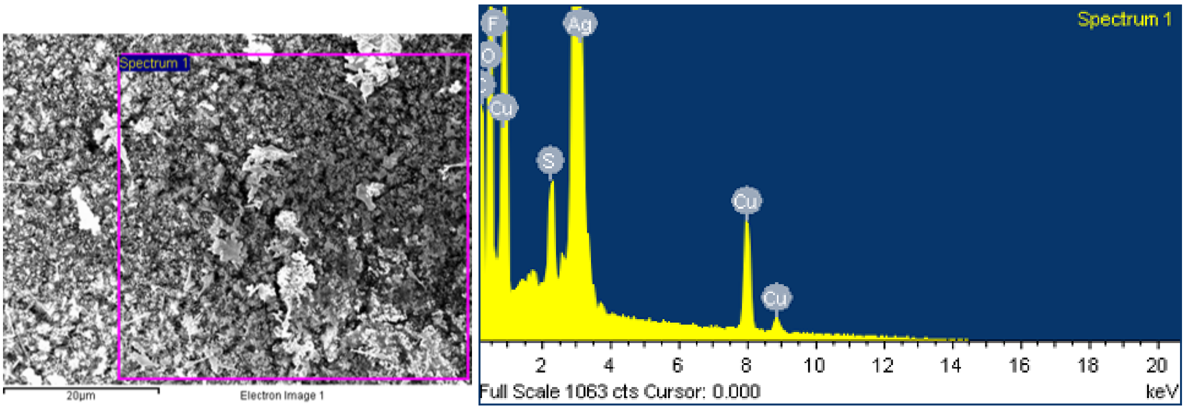

(a) Area defined for EDX scanning

(b) EDX spectrum

Figure 3.28: Sample area (a) and corresponding EDX spectrum (b) for Cu-Ag 3 min.

The values of the Ag/Cu ratios are 0.18 and 0.84 respectively for Cu-Ag 1 min and 3 min. This last data seems to be very strange since it overcomes the ratio found for Cu-Ag 5 min (0.7). It is difficult to understand what this incoherence is due to. Probably, during the synthesis something went wrong and it would be necessary to repeat this sample in the future to get more information. These two new samples show very different topographies among themselves. Cu-Ag 1 min shows a nanostructure more reminiscent of the flower-like morphology seen for Cu 400 s, while Cu-Ag 3 min seems more similar to the micrographs seen for Cu-Ag 75/90°C, in which Ag crystals totally cover the Cu substrate. In both, however, the Cu/Ag-based structures are again observed although it is clear that as the immersion time increases, the size of the same increases as well.

3.3.1 XRD analysis

The XRD spectrum for the three different immersion times studied is shown in Figure 3.29. As might be expected, the crystalline phases present in the three bimetallic catalysts are the same as those indicated in the Subsection 3.2.5. It is possible to see that the peak characteristic of Ag (111) at $2\theta=38°$ has an higher intensity for Cu-Ag 3 min than the two other tested samples. This data confirms that this sample contains much Ag, as confirmed by EDX, which needs to be further studied. In addition, the two peaks of Cu_2O drop in intensity when immersion time increases.

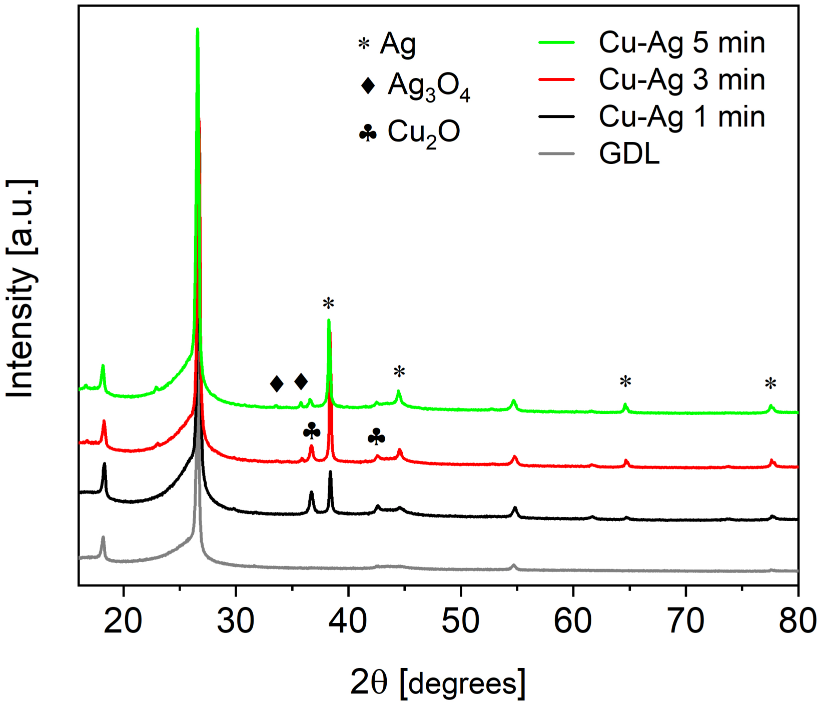

Figure 3.29: XRD spectra for GDL the three bimetallic catalysts synthesized at different immersion times.

CHAPTER 4

Conclusions and future developments

The study carried out on the Cu-Ag bimetallic catalysts, protagonists of this thesis work, has led to promising results. The most important one among these is the higher selectivity toward C_2 products compared with the single Cu-based electrodes. Notwithstanding, several other tests need to be performed in order to better understand the material working mechanism and how its synthesis can be optimized to achieve the best performances. Tuning the intrinsic properties of the material may involve many aspects such as the control of the final surface morphology or the identification of the optimal chemical composition for this application. For instance, an idea to increase specific surface area of the electrode could be to change the sputtered substrate of copper with Cu NPs. In this way, greater CO adsorption on Ag is hoped to obtain and, taking advantage of the high coverage of the surface with these intermediate products, the probability of observing C-C coupling should then increase.

During the preparation of the samples, it became clear that both the temperature and the immersion time, at which the displacement between copper and silver is conducted, affect the behavior during CO_2RR and also the material structure and composition. Despite that, it might be interesting to implement a more in-depth study of the synthesis parameters. Some future projects could be: (i) expanding the investigation of immersion duration: by increasing the dipping time to understand if it is possible to reach better electrochemical performances, by using higher current densities during the galvanostatic tests to compare the results with those obtained from temperature study or also by decreasing the solution T in order to understand the intrinsic effect of immersion time on catalyst behavior; (ii) continuing the work on the solution temperature by changing the immersion time; (iii) starting the investigation of other synthesis parameter like the Ag_2SO_4 solution concentration. One technique that would allow a clearer view of what happens during carbon dioxide reduction is the *electrochemical in situ Raman spectroscopy* which can probe both the catalyst surface and the reaction intermediates present in the catholyte [62]. This kind of characterization is very useful to understand the operation mechanism of the examined class of catalysts and consequently to act on them to optimize their electrochemical performance. The morphology and composition of the studied material certainly shows a relationship to the chosen synthesis parameters. The presence of coarser particles (3.2.4, 3.2.5) on the electrode surface has not yet been explained by the conducted analyses, EDX revealed the presence of Cu and Ag but, being a bulk technique, it is not possible to confirm their composition with certainty. Therefore, it would be interesting to conduct a surface analysis such as XPS (X-ray photoelectron spectroscopy) to clarify the chemical nature of the surface. The XRD spectra also have left doubts about the origin of the more cuprite (Cu_2O), which could be traced back to the coarse particles or to the sputtered Cu substrate that reconstructs itself at $T \geqslant 50°C$. To resolve this issue, the copper electrode could be placed in a heated bath of distilled water only at the interesting temperatures, and then run the XRD analysis again to see whether or not the oxide is present.

In addition, these samples have showed good stability throughout the duration of the electrochemical tests (1 h), especially at lower current densities (200 mA cm^{-2}). It would be very appealing to conduct a stability test to determine if this material can work properly for long periods of time. It is important to remember that the measurement setup adopted can also have an effect on electrocatalytic performance. For example, the GDEs tested at higher currents frequently show the appearance of flooding [63], a phenomenon manifested by the loss of hydrophobicity by the GDL, which makes the CO_2 diffusion from the cathode back to the catalyst[12] more difficult and consequently disfavors the CO_2 reduction and promotes the HER (Figure 4.1). Two possible resolutions to the flooding can be to replace the GDL with a non-carbon-based one or to apply a protective coating that increases carbon paper hydrophobicity while maintaining other essential properties in this component (microporosity and conductivity).

---

[12] deposited on the GDL front side

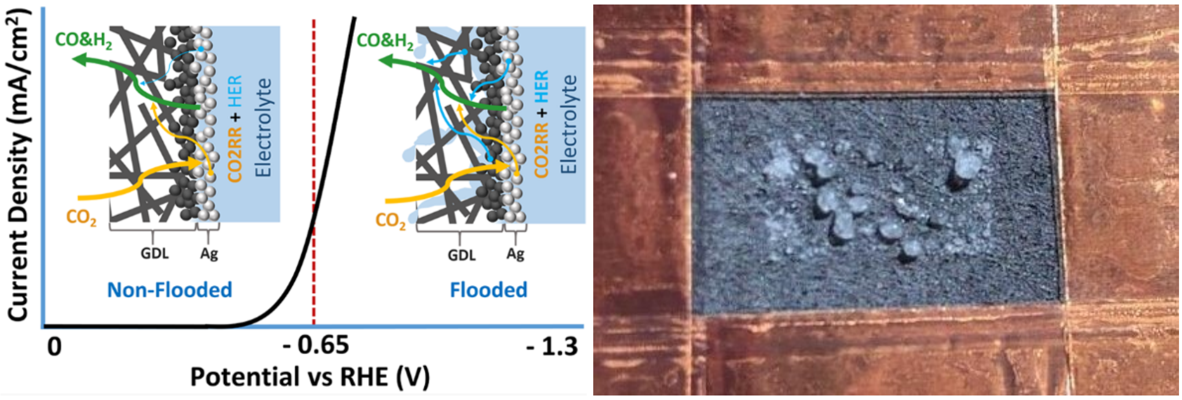

(a) Flooding schematic representation

(b) Real flooding illustration

Figure 4.1: Flooding at different current densities in carbon-based GDLs [63] (a) and real flooding observed on the back of the GDL (b).

Limiting the external factors concerning the measurement environment (flooding, pH and CO_2 concentration effects, product losses, etc.) is essential to isolate the intrinsic mechanism of the catalyst and understand how to optimize it.

Bibliography

[1] Jan Mertens, Christian Breyer, Katrin Arning, André Bardow, Ronnie Belmans, Angela Dibenedetto, Suren Erkman, Jim Gripekoven, Grégoire Léonard, Sylvain Nizou, Deepak Pant, Ana S Reis-Machado, Peter Styring, Jaap Vente, Michael Webber, and Célia J Sapart. Carbon capture and utilization: More than hiding CO_2 for some time. *Joule*, 7(3):442–449, March 2023.

[2] Jan Mertens, Ronnie Belmans, and Michael Webber. Why the carbon-neutral energy transition will imply the use of lots of carbon. *C*, 6(2):39, June 2020.

[3] IEA. Energy Technology Perspectives, 2020. Accessed: 23/08/2023.

[4] Lei Fan, Chuan Xia, Fangqi Yang, Jun Wang, Haotian Wang, and Yingying Lu. Strategies in catalysts and electrolyzer design for electrochemical CO_2 reduction toward C_{2+} products. *Sci. Adv.*, 6(8):eaay3111, February 2020.

[5] Guobin Wen, Bohua Ren, Yun Zheng, Matthew Li, Catherine Silva, Shuqin Song, Zhen Zhang, Haozhen Dou, Lei Zhao, Dan Luo, Aiping Yu, and Zhongwei Chen. Engineering electrochemical surface for efficient carbon dioxide upgrade. *Advanced Energy Materials*, 12(3):2103289, December 2022.

[6] Yuhou Pei, Heng Zhong, and Fangming Jin. A brief review of electrocatalytic reduction of CO_2-Materials, reaction conditions, and devices. *Energy Science Engineering*, 9:1012–1032, June 2021.

[7] Yufei Jia, Fei Li, Ke Fan, and Licheng Sun. Cu-based bimetallic electrocatalysts for CO_2 reduction. *Advanced Powder Materials*, 1(1):100012, October 2022.

[8] Y. Zhong, S. Wang, M. Li, J. Ma, S. Song, A. Kumar, H. Duan, Y. Kuang, and X. Sun. Rational design of copper-based electrocatalysts and electrochemical systems for CO_2 reduction: From active sites engineering to mass transfer dynamics. *Materials Today Physics*, 18:100354, May 2021.

[9] Hemma Mistry, Ana Sofia Varela Gasque, Cecile Bonifacio, Ioannis Zegkinoglou, Ilya Sinev, Yong-Wook Choi, Kim Kisslinger, Eric Stach, Judith Yang, Peter Strasser, and Beatriz Roldan Cuenya. Highly selective plasma-activated copper

catalysts for carbon dioxide reduction to ethylene. *Nature Communications*, 7: 12123, June 2016.

[10] Cao-Thang Dinh, Thomas Burdyny, Md Golam Kibria, Ali Seifitokaldani, Christine M Gabardo, F Pelayo García de Arquer, Amirreza Kiani, Jonathan P Edwards, Phil De Luna, Oleksandr S Bushuyev, Chengqin Zou, Rafael Quintero-Bermudez, Yuanjie Pang, David Sinton, and Edward H Sargent. CO_2electroreduction to ethylene via hydroxide-mediated copper catalysis at an abrupt interface. *Science*, 360(6390):783–787, May 2018.

[11] R.A. Geioushy, Mazen M. Khaled, Khalid Alhooshani, Abbas S. Hakeem, and A. Rinaldi. Graphene/ZnO/Cu_2O electrocatalyst for selective conversion of CO_2 into n-propanol. *Electrochimica acta*, 245:456–462, May 2017.

[12] Yao Zheng, Anthony Vasileff, Xianlong Zhou, Yan Jiao, Mietek Jaroniec, and Shi-Zhang Qiao. Understanding the roadmap for electrochemical reduction of CO_2 to Multi-Carbon Oxygenates and Hydrocarbons on Copper-Based Catalysts. *Journal of the American Chemical Society*, 141(19):7646–7659, April 2019.

[13] Chaitanya B. Hiragond, Hwapyong Kim, Junho Lee, Saurav Sorcar, Can Erkey, and Su-Il In. Electrochemical CO_2 Reduction to CO Catalyzed by 2D Nanostructures. *Catalysts*, 10(1), January 2020.

[14] Shuyu Liang, Naveed Altaf, Liang Huang, Yanshan Gao, and Qiang Wang. Electrolytic cell design for electrochemical CO_2 reduction. *Journal of CO_2 utilization*, 35:90–105, January 2020.

[15] Devin T Whipple, Eryn C Finke, and Paul J A Kenis. Microfluidic reactor for the electrochemical reduction of carbon dioxide: The effect of pH. *Electrochem. Solid State Letters*, 13(9):B109, June 2010.

[16] Jinli Qiao, Yuyu Liu, Feng Hong, and Jiujun Zhang. A Review of Catalysts for the Electroreduction of Carbon Dioxide to Produce Low-Carbon Fuels. *Chemical Society Reviews*, 43:631–675, April 2014.

[17] Otmane Zoubir, Lahoucine Atourki, Hassan Ait Ahsaine, and Amal BaQais. Current state of copper-based bimetallic materials for electrochemical CO_2 reduction: a review. *RSC advances*, 12(46):30056–30075, October 2022.

[18] Jong Suk Yoo, Rune Christensen, Tejs Vegge, Jens Nørskov, and Felix Studt. Theoretical Insight into the Trends that Guide the Electrochemical Reduction of Carbon Dioxide to Formic Acid. *ChemSusChem*, 9(4):358–363, February 2016.

[19] Ruud Kortlever, Jing Shen, K J P Schouten, Federico Calle-Vallejo, and Marc Koper. Catalysts and Reaction Pathways for the Electrochemical Reduction of

Carbon Dioxide. *The Journal of Physical Chemistry Letters*, 6:4073–4082, September 2015.

[20] Yoshio Hori, Katsuhei Kikuchi, and Shin Suzuki. Production of CO and CH_4 in electrochemical reduction of CO_2 at metal electrodes in aqueous hydrogencarbonate solution. *Chemistry Letters - CHEM LETT*, 14:1695–1698, November 1985.

[21] Ifan E L Stephens, Karen Chan, Alexander Bagger, Shannon W Boettcher, Julien Bonin, Etienne Boutin, Aya K Buckley, Raffaella Buonsanti, Etosha R Cave, Xiaoxia Chang, See Wee Chee, Alisson H M da Silva, Phil de Luna, Oliver Einsle, Balázs Endrődi, Maria Escudero-Escribano, Jorge V Ferreira de Araujo, Marta C Figueiredo, Christopher Hahn, Kentaro U Hansen, Sophia Haussener, Sara Hunegnaw, Ziyang Huo, Yun Jeong Hwang, Csaba Janáky, Buddhinie S Jayathilake, Feng Jiao, Zarko P Jovanov, Parisa Karimi, Marc T M Koper, Kendra P Kuhl, Woong Hee Lee, Zhiqin Liang, Xuan Liu, Sichao Ma, Ming Ma, Hyung-Suk Oh, Marc Robert, Beatriz Roldan Cuenya, Jan Rossmeisl, Claudie Roy, Mary P Ryan, Edward H Sargent, Paula Sebastián-Pascual, Brian Seger, Ludmilla Steier, Peter Strasser, Ana Sofia Varela, Rafaël E Vos, Xue Wang, Bingjun Xu, Hossein Yadegari, and Yuxiang Zhou. 2022 roadmap on low temperature electrochemical CO_2 reduction. *J. Phys. Energy*, 4(4):042003, October 2022.

[22] Andrew A Peterson, Frank Abild-Pedersen, Felix Studt, Jan Rossmeisl, and Jens K Nørskov. How copper catalyzes the electroreduction of carbon dioxide into hydrocarbon fuels. *Energy Environ. Sci.*, 3(9):1311–1315, June 2010.

[23] Y. Li, Ziyun Wang, Tiange Yuan, Dae-Hyun Nam, Mingchuan Luo, Joshua Wicks, Bin Chen, Jun Li, Fengwang Li, F. Pelayo García de Arquer, Ying Wang, Cao Thang Dinh, Oleksandr Voznyy, David Sinton, and Edward Sargent. Binding Site Diversity Promotes CO_2 Electroreduction to Ethanol. *Journal of the American Chemical Society*, 141:8584–8591, May 2019.

[24] Anthony Vasileff, Chaochen Xu, Yan Jiao, Yao Zheng, and Shi-Zhang Qiao. Surface and Interface Engineering in Copper-Based Bimetallic Materials for Selective CO_2 Electroreduction. *Chem*, 4(8):1809–1831, August 2018.

[25] Juqin Zeng, Manlio Mignosa, Nicolò B.D. Monti, Adriano Sacco, and Candido F. Pirri. Engineering copper nanoparticle electrodes for tunable electrochemical reduction of carbon dioxide. *Electrochimica acta*, 464:142862, July 2023.

[26] Qilong Wu, Chuangwei Liu, Xiaozhi Su, Qi Yang, Xiaotong Wu, Haiyuan Zou, Baihua Long, Xiaokun Fan, Yujia Liao, Lele Duan, Zewei Quan, and Shuiping Luo. Defect-Engineered Cu-Based Nanomaterials for Efficient CO_2 Reduction over Ultrawide Potential Window. *ACS nano*, 17(1):402–410, December 2023.

[27] Woong Hee Lee, Chulwan Lim, Si Young Lee, Keun Hwa Chae, Chang Hyuck Choi, Ung Lee, Byoung Koun Min, Yun Jeong Hwang, and Hyung-Suk Oh. Highly selective and stackable electrode design for gaseous CO_2 electroreduction to ethylene in a zero-gap configuration. *Nano Energy*, 84:105859–105868, February 2021.

[28] Zhengxiang Gu, Hao Shen, Zheng Chen, Yaoyue Yang, Chao Yang, Yali Ji, Yuhang Wang, Chan Zhu, Junlang Liu, Jun Li, Tsun-Kong Sham, Xin Xu, and Gengfeng Zheng. Efficient Electrocatalytic CO_2 Reduction to C_{2+} Alcohols at Defect-Site-Rich Cu Surface. *Joule*, 5(2):429–440, February 2021.

[29] Chenyuan Zhu, Zhibin Zhang, Lixiang Zhong, Chia-Shuo Hsu, Xiaozhi Xu, Yingzhou Li, Siwen Zhao, Shaohua Chen, Jiayi Yu, Shulin Chen, Mei Wu, Peng Gao, Shuzhou Li, Hao Ming Chen, Kaihui Liu, and Liming Zhang. Product-Specific Active Site Motifs of Cu for Electrochemical CO_2 Reduction. *Chem*, 7(2): 406–420, February 2021.

[30] Ying Chuan Tan, Kelvin Berm Lee, Hakhyeon Song, and Jihun Oh. Modulating Local CO_2 Concentration as a General Strategy for Enhancing CC Coupling in CO_2 Electroreduction. *Joule*, 4(5):1104–1120, May 2020.

[31] Cheonghee Kim, Fabio Dionigi, Vera Beermann, Xingli Wang, Tim Möller, and Peter Strasser. Alloy Nanocatalysts for the Electrochemical Oxygen Reduction (ORR) and the Direct Electrochemical Carbon Dioxide Reduction Reaction (CO_2RR). *Advanced Materials*, 31(31):1805617, August 2019.

[32] Takuya Tsujiguchi, Yusuke Kawabe, Samuel Jeong, Tatsuhiko Ohto, Suresh Kukunuri, Hirotaka Kuramochi, Yasufumi Takahashi, Tomohiko Nishiuchi, Hideki Masuda, Mitsuru Wakisaka, Kailong Hu, Ganesan Elumalai, Jun-ichi Fujita, and Yoshikazu Ito. Acceleration of Electrochemical CO_2 Reduction to Formate at the Sn/Reduced Graphene Oxide Interface. *ACS catalysis*, 11(6):3310–3318, March 2021.

[33] Tian Wang, Jiadong Chen, Xinyi Ren, Jincheng Zhang, Jie Ding, Yuhang Liu, Kang Hui Lim, Junhu Wang, Xuning Li, Hongbin Yang, Yanqiang Huang, Sibudjing Kawi, and Bin Liu. Halogen-Incorporated Sn Catalysts for Selective Electrochemical CO_2 Reduction to Formate. *Angewandte Chemie (International ed.)*, 62 (10):e202211174, January 2023.

[34] Shahid Rasul, Dalaver H. Anjum, Abdesslem Jedidi, Yury Minenkov, Luigi Cavallo, and Kazuhiro Takanabe. A Highly Selective Copper-Indium Bimetallic Electrocatalyst for the Electrochemical Reduction of Aqueous CO_2 to CO. *Angewandte Chemie (International ed.)*, 54(7):2146–2150, February 2015.

[35] Chenqi Shen, Pengtang Wang, Leigang Li, Xiaoqing Huang, and Qi Shao. Phase and structure modulating of bimetallic Cu/In nanoparticles realizes efficient electrosynthesis of syngas with wide CO/H_2 ratios. *Nano research*, 15(1):528–534, January 2022.

[36] Jiazheng Ren, Xia Long, Xiaoting Wang, Zedong Lin, Rongming Cai, Min Ju, Yongfu Qiu, and Shihe Yang. Defect-Rich Heterostructured Bi-Based Catalysts for Efficient CO_2 Reduction Reaction to Formate in Wide Operable Windows. *Energy Technology (Weinheim, Germany)*, 10(10):2200561, October 2022.

[37] Xueli Wang, Lu-Hua Zhang, Datong Chen, Jiayu Zhan, Jiangyi Guo, Zisheng Zhang, and Fengshou Yu. Enhanced Electroconversion CO_2-to-Formate by Oxygen-Vacancy-Rich Ultrasmall Bi-Based Catalyst Over a Wide Potential Window. *ChemCatChem*, 14(6):e202101873, March 2022.

[38] Yiqun Zheng, Jiawei Zhang, Zesong Ma, Gongguo Zhang, Haifeng Zhang, Xiaowei Fu, Yanyun Ma, Feng Liu, Maochang Liu, and Hongwen Huang. Seeded Growth of Gold–Copper Janus Nanostructures as a Tandem Catalyst for Efficient Electroreduction of CO_2 to C_{2+} Products. *Small (Weinheim an der Bergstrasse, Germany)*, 18(19):2201695, April 2022.

[39] Douglas R Kauffman, Dominic R Alfonso, De Nyago Tafen, Congjun Wang, Yunyun Zhou, Yang Yu, Jonathan W Lekse, Xingyi Deng, Vanessa Espinoza, Jamie Trindell, Oshadha K Ranasingha, Amitava Roy, Jun-Sik Lee, and Huolin L Xin. Selective Electrocatalytic Reduction of CO_2 into CO at Small, Thiol-Capped Au/Cu Nanoparticles. *Journal of Physical Chemistry C*, 122(49):27991–28000, August 2018.

[40] Chubai Chen, Yifan Li, Sunmoon Yu, Sheena Louisia, Jianbo Jin, Mufan Li, Michael B. Ross, and Peidong Yang. Cu-Ag Tandem Catalysts for High-Rate CO_2 Electrolysis toward Multicarbons. *Joule*, 4(8):1688–1699, August 2020.

[41] Jianfeng Huang, Mounir Mensi, Emad Oveisi, Valeria Mantella, and Raffaella Buonsanti. Structural sensitivities in bimetallic catalysts for electrochemical co2 reduction revealed by ag–cu nanodimers. *Journal of the American Chemical Society*, 141(6):2490–2499, January 2019.

[42] Ezra L Clark, Christopher Hahn, Thomas F Jaramillo, and Alexis T Bell. Electrochemical CO_2 Reduction over Compressively Strained CuAg Surface Alloys with Enhanced Multi-Carbon Oxygenate Selectivity. *Journal of the American Chemical Society*, 139(44):15848–15857, October 2017.

[43] Laxia Wu, Lin Wu, Chang Guo, Yebin Guan, Huan Wang, and Jiaxing Lu. Progress in Electroreduction of CO_2 to Form Various Fuels Based on Zn Catalysts. *Processes*, 11(4):1039, March 2023.

[44] Hyo Sang Jeon, Ilya Sinev, Fabian Scholten, Nuria J Divins, Ioannis Zegkinoglou, Lukas Pielsticker, and Beatriz Roldan Cuenya. Operando Evolution of the Structure and Oxidation State of Size-Controlled Zn Nanoparticles during CO_2 Electroreduction. *Journal of the American Chemical Society*, 140(30):9383–9386, July 2018.

[45] Bo Xiong, Jing Liu, Yingju Yang, Yuchen Yang, and Zhixuan Hua. Effect mechanism of NO on electrocatalytic reduction of CO_2 to CO over Pd@Cu bimetal catalysts. *Fuel (Guildford)*, 323:124339–, April 2022.

[46] Lu Lu, Xiaofu Sun, Jun Ma, Dexin Yang, Haihong Wu, Bingxing Zhang, Jianling Zhang, and Buxing Han. Highly Efficient Electroreduction of CO_2 to Methanol on Palladium–Copper Bimetallic Aerogels. *Angewandte Chemie (International ed.)*, 57(43):14149–14153, October 2018.

[47] Chan Woo Lee, Ki Dong Yang, Dae-Hyun Nam, Jun Ho Jang, Nam Heon Cho, Sang Won Im, and Ki Tae Nam. Defining a Materials Database for the Design of Copper Binary Alloy Catalysts for Electrochemical CO_2 Conversion. *Advanced materials (Weinheim)*, 30(42):1704717, January 2018.

[48] Zhiyuan Chang, Shengjuan Huo, Wei Zhang, Jianhui Fang, and Hailiang Wang. The Tunable and Highly Selective Reduction Products on Ag@Cu Bimetallic Catalysts Toward CO2 Electrochemical Reduction Reaction. *Journal of physical chemistry. C*, 121(21):11368–11379, May 2017.

[49] Jie Zhang, Thi Ha My Pham, Youngdon Ko, Mo Li, Shuliang Yang, Cedric David Koolen, Liping Zhong, Wen Luo, and Andreas Züttel. Tandem effect of Ag@C@Cu catalysts enhances ethanol selectivity for electrochemical CO_2 reduction in flow reactors. *Cell Reports Physical Science*, 3(7):100949, July 2022.

[50] Yongzhi Zhong, Xiangdong Kong, Zhimin Song, Yan Liu, Liping Peng, Lin Zhang, Xuan Luo, Jie Zeng, and Zhigang Geng. Adjusting Local CO Confinement in Porous-Shell Ag@Cu Catalysts for Enhancing C-C Coupling toward CO_2 Eletroreduction. *Nano letters*, 22(6):2554–2560, February 2022.

[51] Meng Li, Yue Hu, Gang Dong, Tianci Wu, and Dongsheng Geng. Achieving Tunable Selectivity and Activity of CO_2 Electroreduction to CO via Bimetallic Silver–Copper Electronic Engineering. *Small (Weinheim an der Bergstrasse, Germany)*, 19(15):2207242, January 2023.

[52] Tianyu Zhang, Justin C Bui, Zhengyuan Li, Alexis T Bell, Adam Z Weber, and Jingjie Wu. Highly selective and productive reduction of carbon dioxide to multicarbon products via in situ CO management using segmented tandem electrodes. *Nature Catalysis*, 5(3):202–211, March 2022.

[53] Hailing Wang, Xiangji Zhou, Tianshui Yu, Xianglong Lu, Lihua Qian, Pan Liu, and Pengxiang Lei. Surface restructuring in AgCu single-atom alloy catalyst and self-enhanced selectivity toward CO_2 reduction. *Electrochimica Acta*, 426:140774, September 2022.

[54] Abhijit Dutta, Iván Zelocualtecatl Montiel, Rolf Erni, Kiran Kiran, Motiar Rahaman, Jakub Drnec, and Peter Broekmann. Activation of bimetallic AgCu foam electrocatalysts for ethanol formation from CO_2 by selective Cu oxidation/reduction. *Nano Energy*, 68:104331, 2020.

[55] Nicolo B. D. Monti, Marco Fontana, Adriano Sacco, Angelica Chiodoni, Andrea Lamberti, Candido F. Pirri, and Juqin Zeng. Facile Fabrication of Ag Electrodes for CO_2-to-CO Conversion with Near-Unity Selectivity and High Mass Activity. *ACS Applied Energy Materials*, 5(12):14779–14788, November 2022.

[56] Reza Azadbakht, Saeid Menati, Hadi Amiri Rudbari, and Mohammad Mahdi Keypour. Deposited Silver Nanoparticles on Commercial Copper by Galvanic Displacement as an Effective Catalyst for the Reduction of 4-Nitrophenol in Aqueous Solution. *Catalysis letters*, 150(11):3214–3222, April 2020.

[57] Angshuman Pal, Panart Khajornrungruang, Christopher Netzband, Sriveda Alety, and S V Babu. Observation of the formation of anisotropic silver microstructures by evanescent wave and electron microscopy. *Nanotechnology*, 27(7):075708, January 2016.

[58] P. Spitzer, S. Wunderli, K. Maksymiuk, A. Michalska, A. Kisiel, Z. Galus, and G. Tauber. Chapter 5 - Reference Electrodes for Aqueous Solutions. In György Inzelt, Andrzej Lewenstam, and Fritz Scholz, editors, *Handbook of reference electrodes*, page 87. Springer Berlin Heidelberg, Berlin, Heidelberg, April 2013.

[59] M. Abd Mutalib, M.A. Rahman, M.H.D. Othman, A.F. Ismail, and J. Jaafar. Chapter 9 - Scanning Electron Microscopy (SEM) and Energy-Dispersive X-Ray (EDX) Spectroscopy. In Nidal Hilal, Ahmad Fauzi Ismail, Takeshi Matsuura, and Darren Oatley-Radcliffe, editors, *Membrane Characterization*, pages 161–179. Elsevier B.V, February 2017.

[60] Alper Koçak. Thin Film Preparation, Particle Size and Thickness Analysis. , Anadolu University, Materials Science and Engineering, Experimental Report, February 2018.

[61] Amrut Lanje, Satish Sharma, and Ramchandra Pode. Synthesis of silver nanoparticles: A safer alternative to conventional antimicrobial and antibacterial agents. *J. Chem. Pharm. Res.*, 2:478–483, January 2010.

[62] Hefei Li, Pengfei Wei, Dunfeng Gao, and Guoxiong Wang. In situ Raman spectroscopy studies for electrochemical CO_2 reduction over Cu catalysts. *Current Opinion in Green and Sustainable Chemistry*, 34:100589, April 2022.

[63] Kailun Yang, Recep Kas, Wilson A. Smith, and Thomas Burdyny. Role of the Carbon-Based Gas Diffusion Layer on Flooding in a Gas Diffusion Electrode Cell for Electrochemical CO_2 Reduction. *ACS Energy Letters*, 6(1):33–40, January 2021.